D0-Note 3405
February 1998

Analysis of the SMT Beam Tests Data

Maria Teresa P. Roco*
Fermi National Accelerator Laboratory
Batavia, IL. 60510-0500

ABSTRACT

Extensive tests of the D-Zero silicon vertex detectors instrumented with the final version of the SVX-II chip and readout electronics were performed at a test beam facility equipped with a 2 Tesla magnet at FNAL. Results are reported on the performance of the SVX-II chip, charge collection properties, signal to noise ratio, cluster pulse height and spatial resolution.

1 Introduction

Recently extensive tests of the D0 silicon detectors have been performed at a test beam at Fermilab. Several single-sided silicon detectors were tested with the final version of the SVX-II chip and the readout electronics. The detectors were operated at both 396 and 132 ns interaction modes. Results on the performance of the SVX-II chip, charge collection properties, signal to noise ratio, cluster pulse height and spatial resolution are presented for the single-sided test ladders. Studies on radiation damage effects based on tests performed on a previously irradiated detector are also shown. Preliminary results on the SMT beam tests data were presented at VERTEX '97 [1].

2 Test Devices and Experimental Setup

The test devices included four beam telescope elements using six single-sided 50 μm pitch silicon detectors operating at 35 V bias voltage. They are fabricated on n-type silicon of 300 μm thickness. Each detector has 384 strips read out by three 128-channel SVX-II chips. The detectors are AC-coupled to the readout electronics by capacitors integrated directly onto each strip. The coupling capacitor is formed by a 200 nm dielectric (SiO_2) layer between the strip implant and the Al metalization. Polysilicon resistors (2 $M\Omega$) are used to bias the strips.

*e-mail address: roco@fnal.gov

Beam tests were performed at Fermilab N-West (NWA) with a 125 GeV charged pion beam. The test beam setup is shown schematically in Fig. 1. Four detectors were used as vertical sensors (v) and two were used as horizontal sensors (h) providing six space points in x and y to measure the trajectory of the incoming beam particle. The coincidence of four scintillator counters located upstream and downstream of the telescope elements provided the beam trigger. To simulate the superconducting solenoid in the upgraded detector, the test beam setup included a magnet which can provide a $\vec{B}$ field of up to 2 Tesla. The magnetic field is in the direction parallel to the detector strips.

A test ladder, constructed by wire-bonding two detectors together, is mounted on a remotely controlled movable table allowing rotation around the vertical axis as well as translation in the horizontal and vertical directions perpendicular to the beam. Rotations around the horizontal axis are done manually. The reference frame is shown in Fig. 2 with the z-axis along the beam direction. The x-axis is parallel to detector strips.

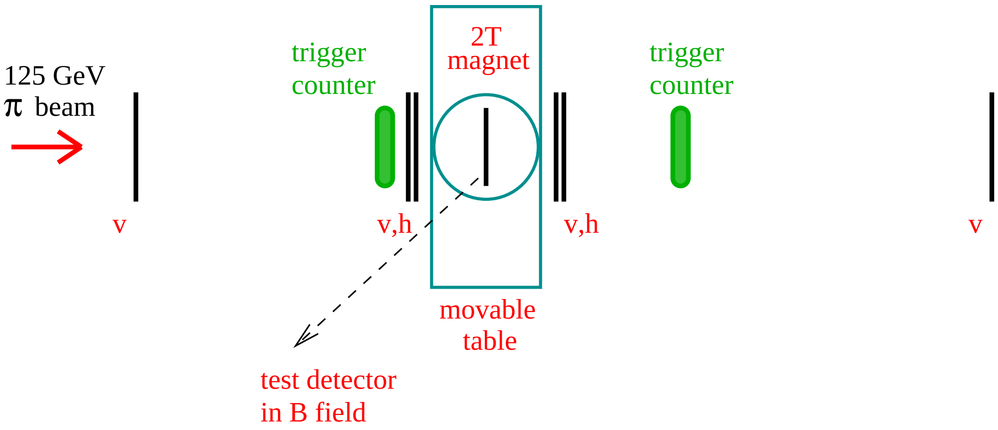

Figure 1: *Test beam setup. Shown are four telescope elements (denoted by v or h) and a remotely controlled movable table where test detectors are mounted.*

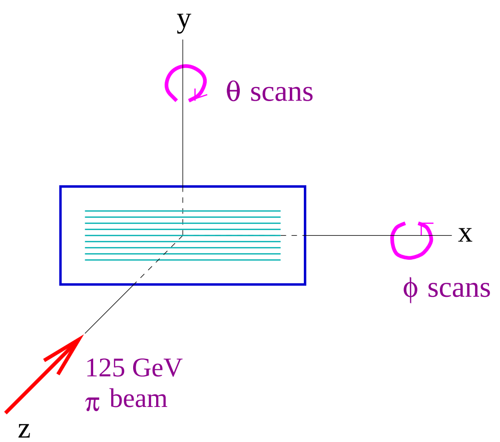

Figure 2: *The z-axis is parallel to the beam direction, while the x-axis is parallel to the detector strips. Data were taken with the plane of the test detector rotated for several values of θ and ϕ. The magnetic field is in the direction parallel to the detector strips and can be varied up to 2 Tesla.*

3 Data Analysis

During the passage of a particle across a silicon detector, the charge generated by the ionization mechanism is collected by one or more adjacent strips. A selection criteria described below is applied to separate clusters generated by tracks from 'fake' clusters due to noise. The plot in Fig. 3 shows the ratio of the baseline and pedestal corrected pulse height to the random noise σ_N for all 128 channels in a chip for data with beam (points) and without beam (hatched). One can clearly separate the signal from noise with the following selection criteria: the corrected pulse heights of all channels are scanned for any signal larger than five times the random noise σ_N of the channel. A cluster charge is defined as the sum of this signal and the signals of all contiguous channels i above $2\sigma_N^i$. The cluster position is defined as the charge centroid, $y_{cog} = \frac{\sum_i Q_i y_i}{\sum_i Q_i}$, where the sum is over all the constituent strips. Clusters which include bad channels are excluded.

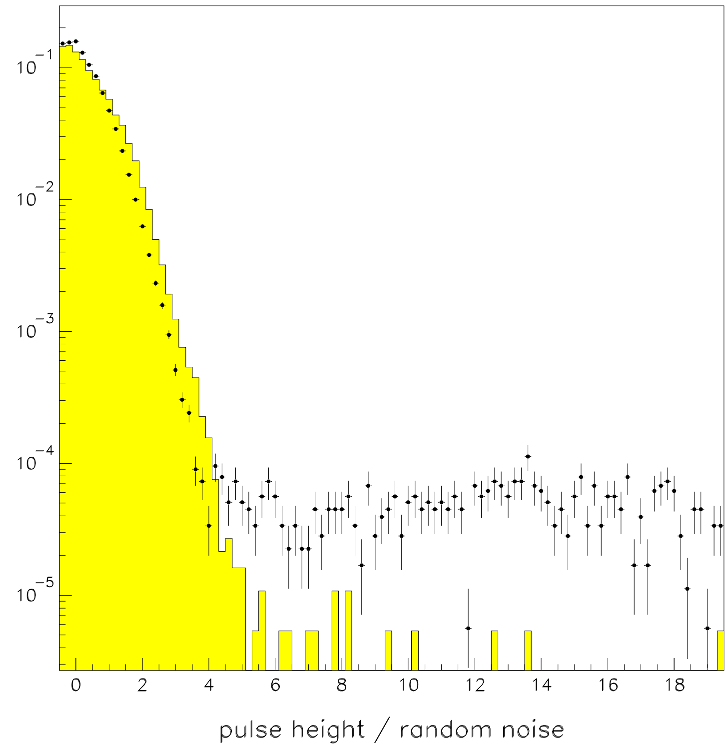

Figure 3: *The ratio of the pulse height to the random noise for all 128 channels of a chip for a pedestal run taken without beam (shown as the hatched histogram) and with beam (shown as the points). The criteria to separate signal from noise is based on this ratio.*

3.1 Common Mode Noise

The common mode baseline shift is obtained for a given SVX chip on an event by event basis by taking the average of the raw pulse height distribution of all 128 channels. This distribution is shown in Fig. 4 for a typical event. The baseline shift is subtracted from the pulse height of each channel and the residual is averaged over the entire run (typically ~ 2500 events) to obtain the pedestal and its root mean square for each channel.

The fluctuation of this baseline from event to event is referred to as the common mode or coherent noise. Plotting the raw pulse height distribution of a single channel for all events in a single data-taking run, as shown in Fig. 5, the common mode noise for this channel is given by the width of a Gaussian function fitted to this distribution. On average the channel to channel variation of the common mode noise across the test ladder, excluding noisy channels, is less than 3 ADC counts as seen in the bottom plot of Fig. 5.

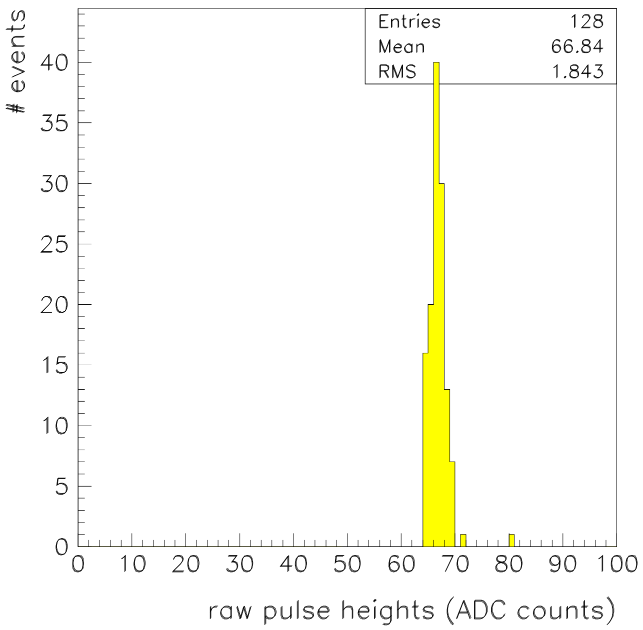

Figure 4: *The raw pulse height distribution of all 128 channels of a chip for a typical event. The average pulse height, referred to as the baseline shift, is corrected for by subtracting this average from the raw pulse height of each channel in the chip event by event.*

3.2 Pedestals and Random Noise

A single channel raw pulse height distribution is shown before (top plot) and after (middle plot) the common mode baseline correction in Fig. 6. The pedestal is given by the mean offset from 0.0 ADC count. Also shown (bottom plot) is the baseline and pedestal corrected pulse height distribution now centered around 0.

Pedestals for the telescope element TBT1 are shown in Fig. 7. A rising/falling slope of the pedestals as a function of channel number, observed during the test beam, leads to a channel to channel pedestal variation of up 2 to 3 ADC counts across a single chip. In the data analysis a pedestal correction is applied. Pedestal corrected pulse heights for all channels in the test ladder are shown in Fig. 8.

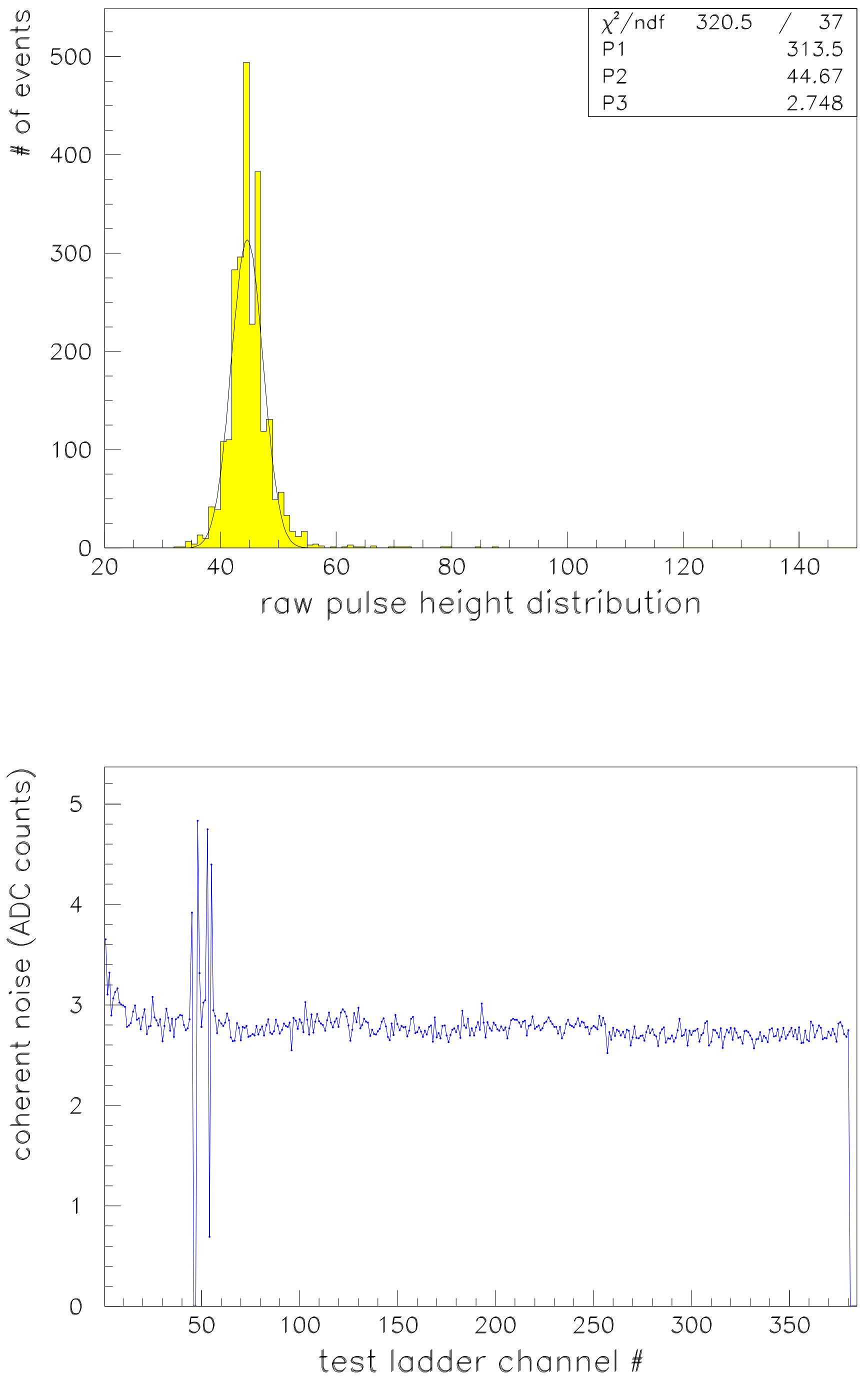

Figure 5: *(top) The raw pulse height distribution of a single channel in a chip. The width of the distribution is a measure of the baseline fluctuation from event to event, referred to as the common mode or coherent noise. (bottom) Common mode noise for all channels in the test ladder.*

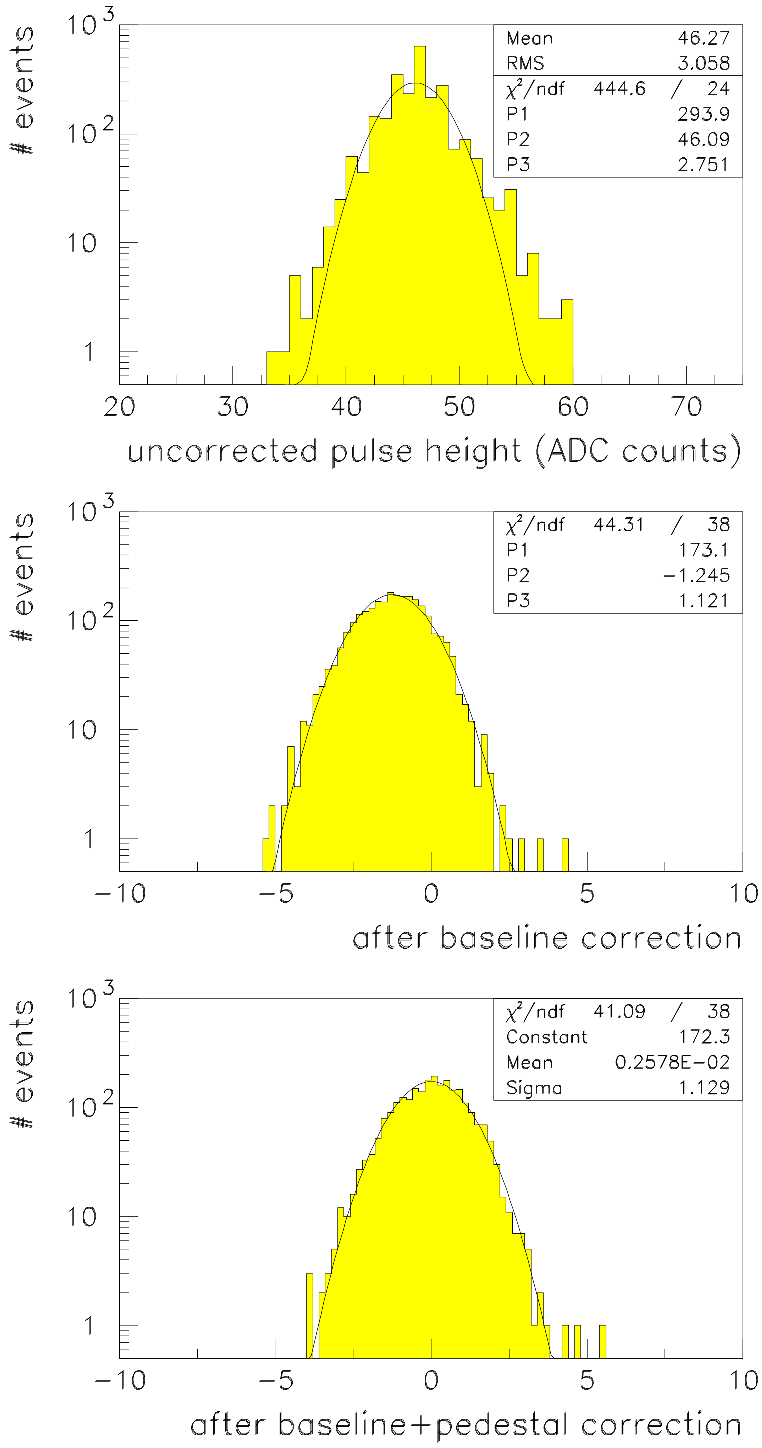

Figure 6: *(top) Uncorrected single channel pulse height distribution. (middle) After the common mode baseline shift correction. (bottom) After baseline and pedestal corrections.*

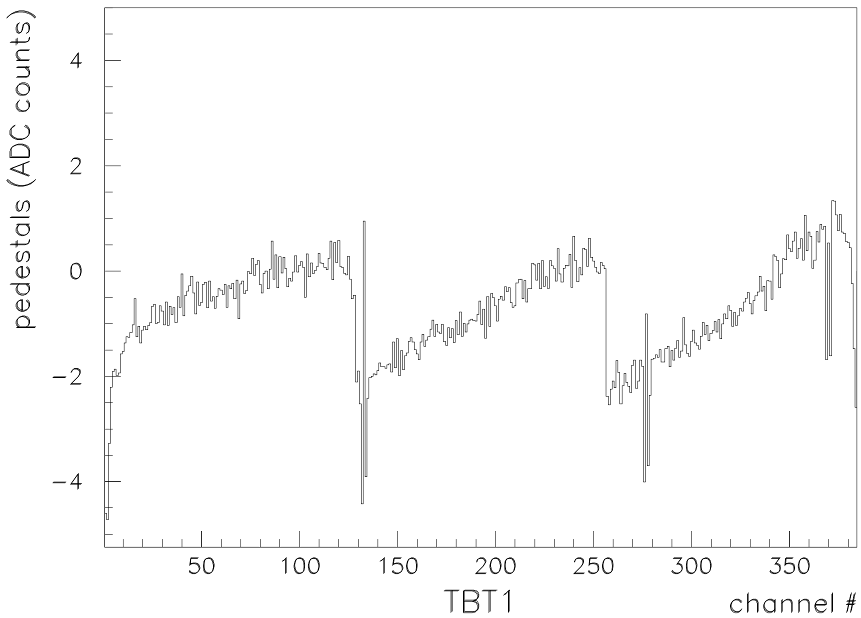

Figure 7: *Pedestals for all channels in the telescope element TBT1.*

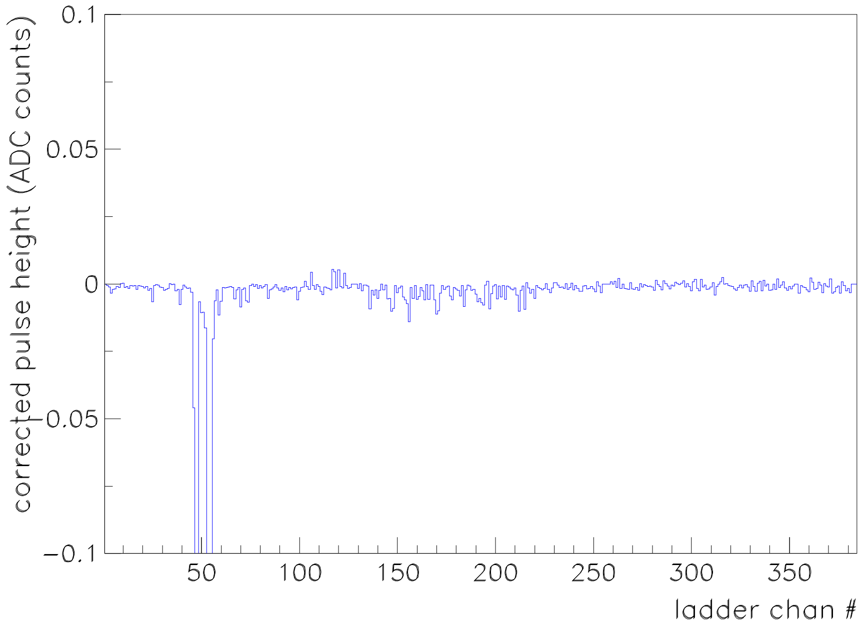

Figure 8: *Pedestal corrected pulse heights for all channels in the test ladder. The two dips around channel 50 are bad channels.*

The width of the distribution in the bottom plot shown in Fig. 6 is referred to as the random noise. In contrast to the common mode noise which is attributed to insufficient grounding and the readout electronics, random noise is uncorrelated and gives a measure of the intrinsic noise of the silicon detector. Fig. 9 shows the random noise for all the channels in the test ladder. Excluding noisy channels the channel to channel variation across the ladder is, on average, less than 0.25 ADC counts. The average random noise is 1.2 ADC counts corresponding to an equivalent noise charge of about 1150 e^{-}.

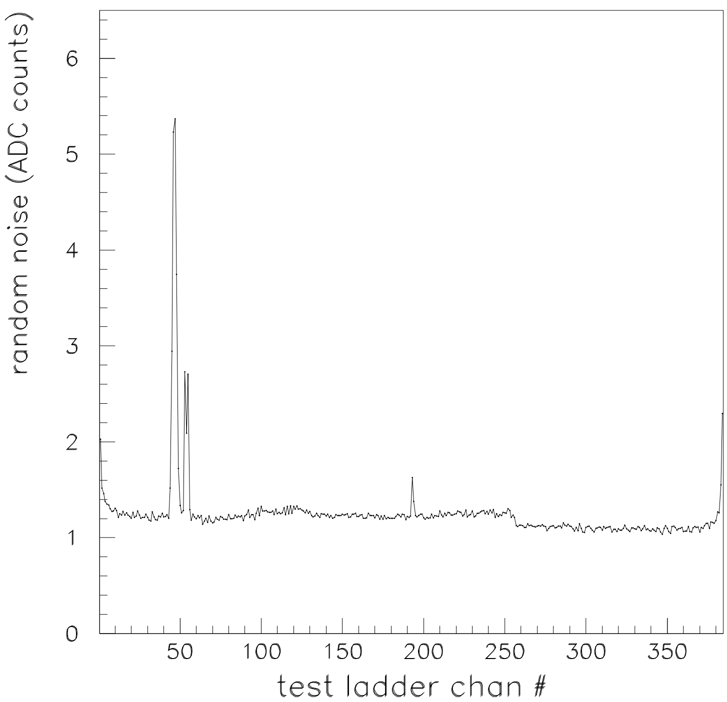

Figure 9: *Random noise for all the channels in the test ladder. The spikes around channel 50 are bad channels*

4 Data Sparsification and Occupancy

In order to understand noise in a beam test environment, data sparsification was not implemented during the data-taking. However, its effects are easily simulated by applying threshold cuts to the data. No cuts were used in generating the following plots in this section. The statistics is based on four successive runs 3034-37 taken in the last week of data-taking, with a total of 12.5 K events.

Fig. 10 shows the raw pulse height distribution of all 128 channels in each of the 3 chips in the test ladder. The distribution is narrower in the third chip because there were no beam particles crossing this segment of the ladder. The fraction of strips that are above a given threshold is shown in Fig. 11 for each chip. The middle of the three lines shown

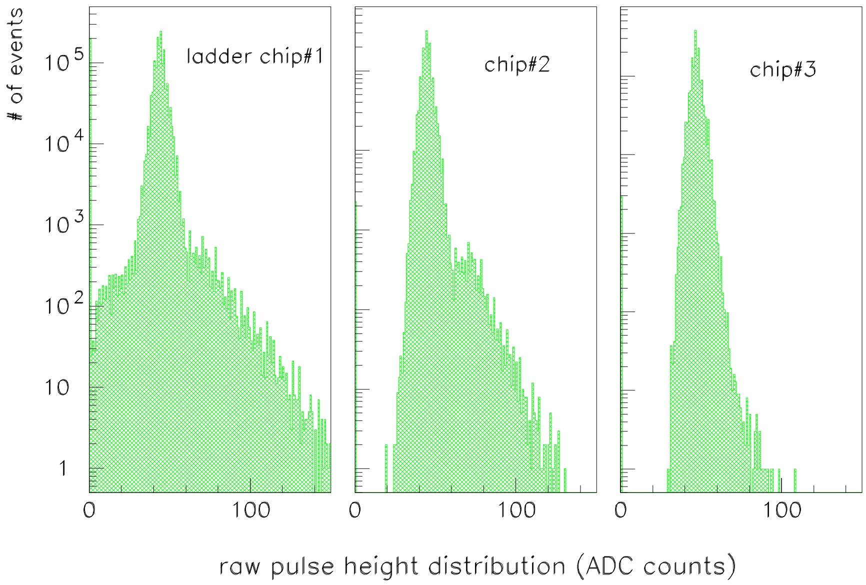

Figure 10: *Raw pulse height distribution of all 128 channels for each chip in the test ladder. Note that the distribution is narrower in the third chip. This is because there were no beam particles crossing this segment of the test ladder.*

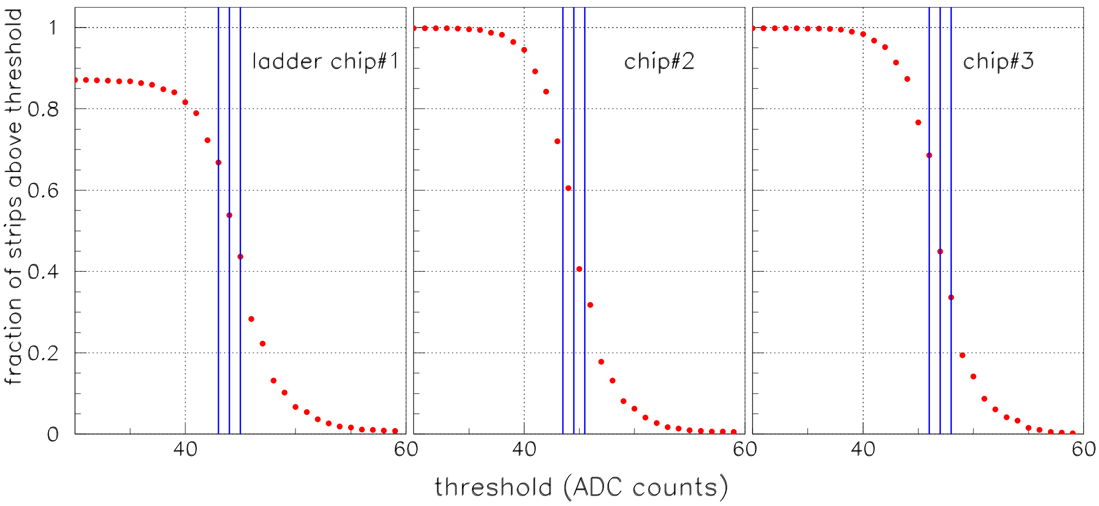

Figure 11: *Fraction of strips that are above threshold for each chip in the test ladder. The middle of the three lines shown corresponds to the average pulse height of 128 channels in that chip. The lines to the left and to the right represent 1 ADC count below and above this average. Due to hardware problems during the test beam, data for some chip ids were actually missing for a fraction of events in a data-taking run. In this sample, runs 3034-37, the missing data amounted to about 13 % of the events for chip 1 in the ladder.*

corresponds to the average pulse height of 128 channels in that chip. One expects that 50 % of the channels are above or below this value. The lines to the left and to the right represent 1 ADC count below and above this average, respectively. For example, if one applies a threshold cut 5 ADC counts above the average value for each chip, 7%, 6% and 4% out of 128 channels for chip 1, 2 and 3, respectively, are above threshold. For comparison, plots for two telescope elements TBT1 and TBT4 are also shown in Fig. 12.

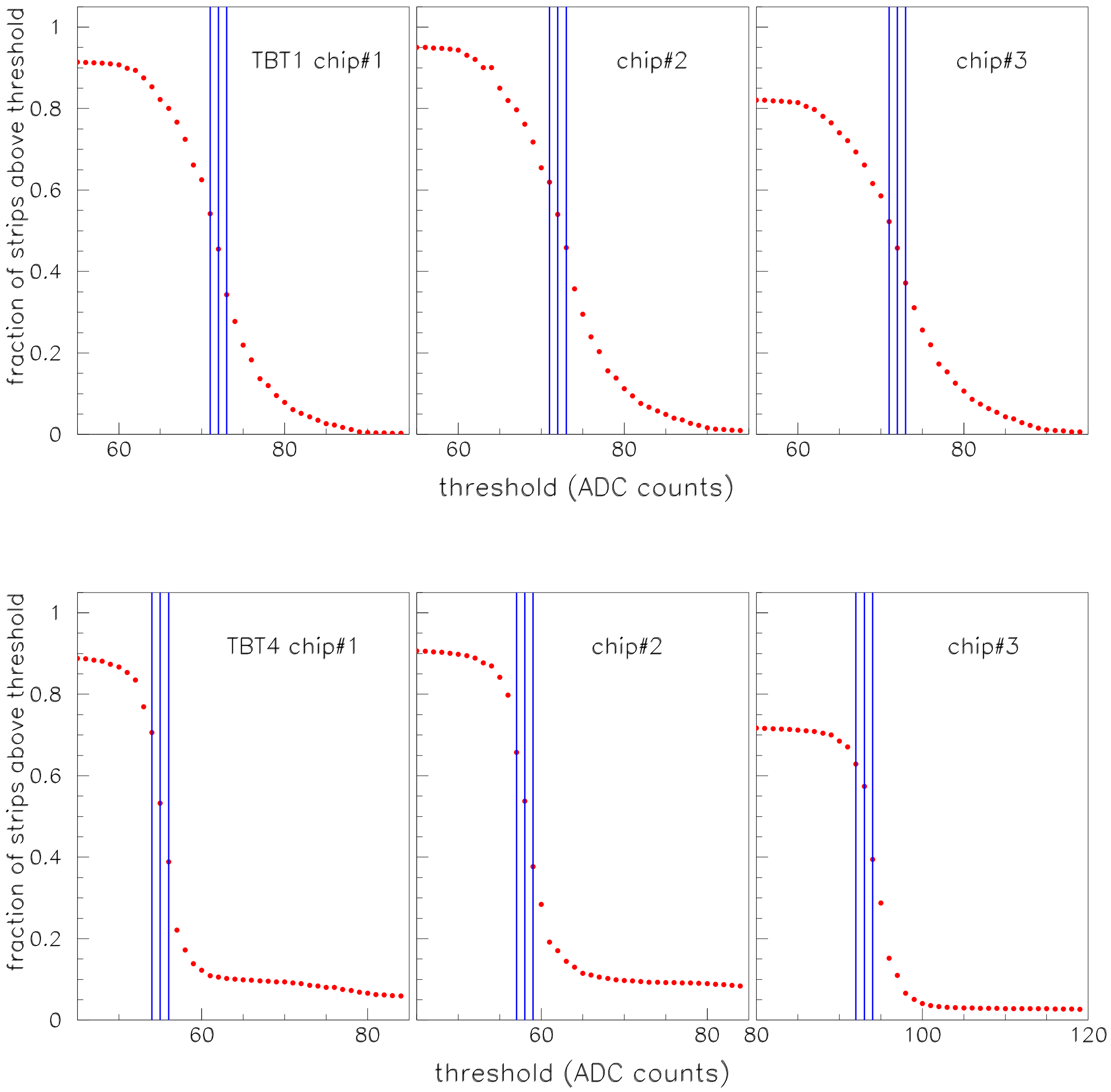

Figure 12: *Fraction of strips that are above threshold for each chip in the telescope elements TBT1 (top) and TBT4 (bottom). The middle of the three lines shown corresponds to the average pulse height of 128 channels in that chip. The lines to the left and to the right represent 1 ADC count below and above this average. Due to a large number of noisy channels in TBT4, the fraction of strips stays constant at large threshold values.*

The telescope elements were noisier than the test ladder. For a threshold cut of 5 ADC counts above the average value for each chip in TBT1, 12%, 16% and 15% out of 128 channels are above threshold. The corresponding numbers for TBT4 are 11%, 13% and 5%. The occupancy, defined as the fraction of strips above threshold, is plotted for the test ladder and separately for the telescope elements in Fig. 13. Based on the ladder performance at threshold above 8 ADC counts (beam at normal incidence, $B = 0$T), the total occupancy is $\sim 2.5\%$ of which 1.5 % is physics occupancy and 1% is due to noise. During the test beam all detectors were operated at room temperature. It is expected that noise should decrease with decreasing temperature. A recent study showing the temperature dependence of noise is presented in [2].

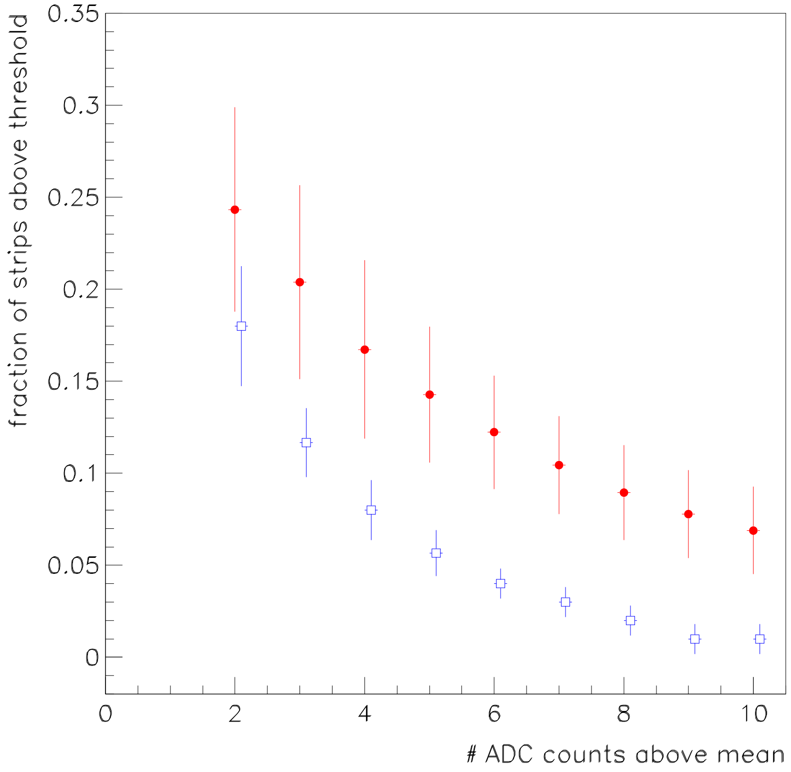

Figure 13: *Occupancy as a function of threshold in the test ladder (shown as the open squares) and the telescope elements (shown as the filled circles).*

5 Signal to Noise Ratio

The cluster charge for normally incident beam particles with $B = 0$T is shown in Fig. 14. The signal to noise ratio S/N is defined as Q_{mp}/σ_N, where Q_{mp} is the most probable value of the cluster charge. To determine Q_{mp} the distribution in Fig. 14 is fitted with a Gaussian convoluted Landau distribution [4] as shown. Since the channel to channel variation of the random noise, σ_N^i, for the same SVX-II chip is small, the average is used in this analysis. A signal to noise ratio of 21 was obtained for the single-sided test ladder. It should be noted that this ratio was obtained under test beam conditions where the test ladder was operated at room temperature. This ratio should improve by at least 10% by operating the detector at lower temperatures.

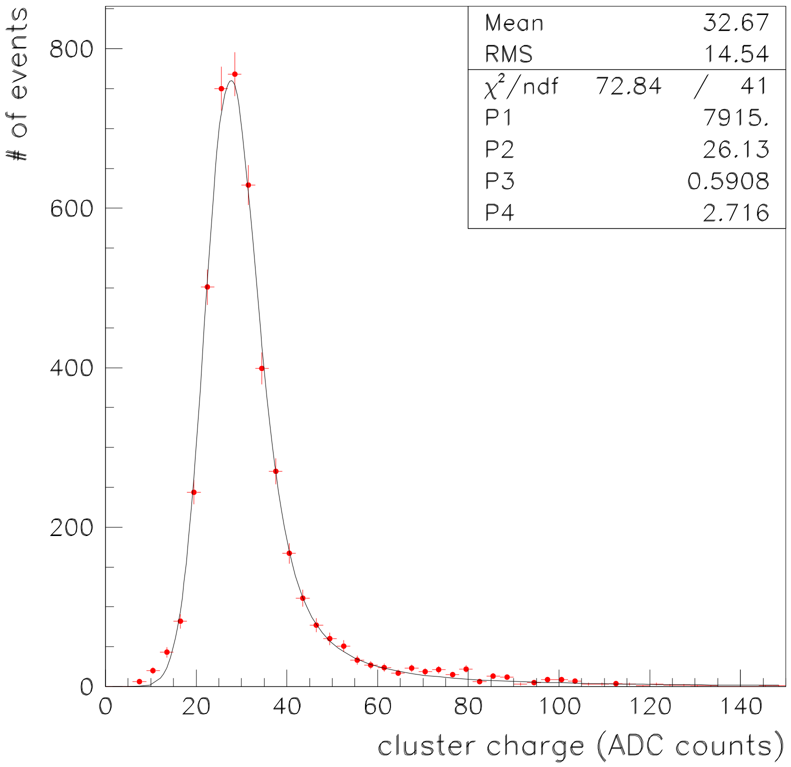

Figure 14: *The cluster charge distribution for the ladder fitted with a Gaussian convoluted Landau function gives a most probable value of 26 ADC counts for 1 mip.*

6 Cluster Profile of Inclined Tracks

In practical applications, tracks impinge on the detectors at arbitrary incidence angles. In the test beam setup the test detector is mounted on a movable table allowing rotations in θ and ϕ. Studies on the angular dependence of cluster charge and size as well as position resolution can be then performed. Data were taken with the plane of the test detector rotated at several values of θ and ϕ as illustrated in Fig. 15.

6.1 Theta Scans

Scans were performed at values of $\theta = 0^o$, 6.1^o, 14.3^o, 22.1^o, 29.1^o, 37.7^o, 45.6^o, 53.4^o, 61.3^o. These scans were repeated at different magnetic field settings from $B = 0$ to 2T. The cluster charge distributions are shown in Fig. 16 for various polar angles of incidence ($B = 0$T and $\phi = 0$). As expected the cluster charge increases with increasing values of θ since the incident particle traverses more silicon material and therefore generates more charge. Ignoring noise and diffusion effects, the passage length goes as $1/\cos\theta$ which results in a $1/\cos\theta$ dependence of the cluster charge. This is verified in Fig. 17 where the most probable value of the cluster charge is plotted as a function of θ for $B = 0$T (shown as the filled circles) and $B = 2$T (shown as the open squares). The data show good agreement with the expected geometric scaling of the charge with $1/\cos\theta$ shown as the dashed curve. The data also show that the cluster charge is independent of the magnetic field.

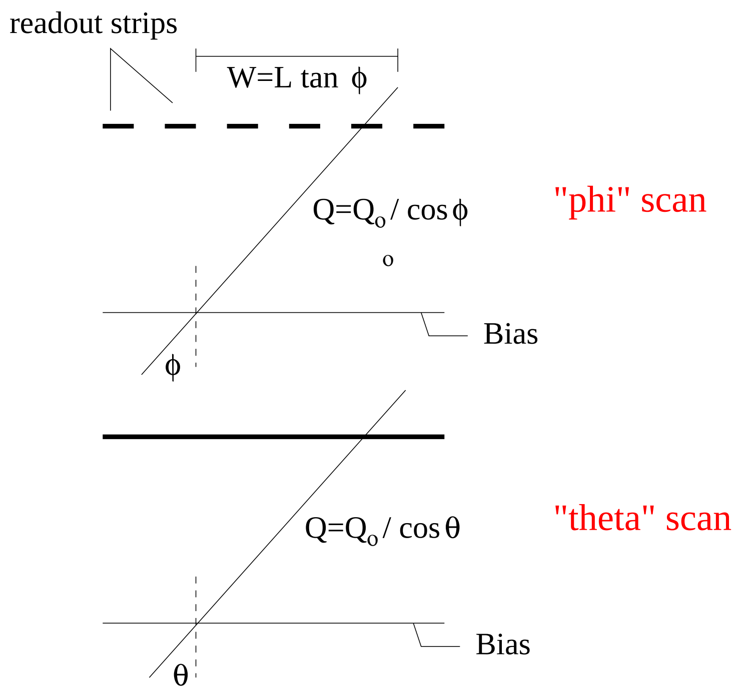

Figure 15: *Track projections are drawn for ϕ and θ scans.*

6.2 Phi Scans

Phi scans were performed at values of $\phi = 0^o$, 10^o, 20^o, 30^o. Note that in Fig. 15, the number of strips that will be traversed by the track should increase proportionately with $\tan\phi$. Not considering noise and charge diffusion, the expected number of strips at 30^o at $B = 0$T is given by the sagitta $W = L\tan\phi = 3.5$ where L is the thickness of the silicon

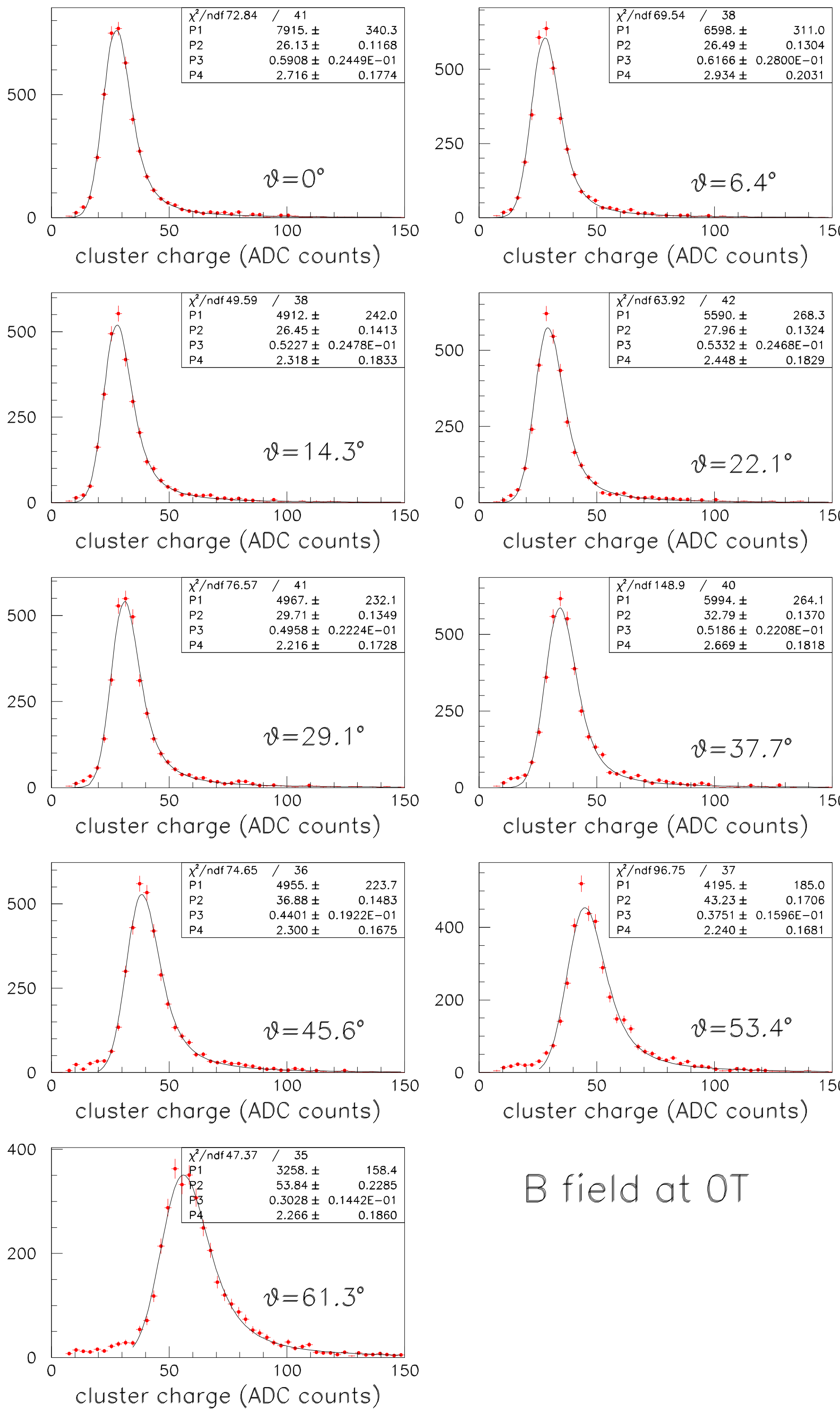

Figure 16: *The cluster charge distribution for the ladder are shown for various polar (θ) angles of incidence at $B = 0T$ and $\phi = 0$.*

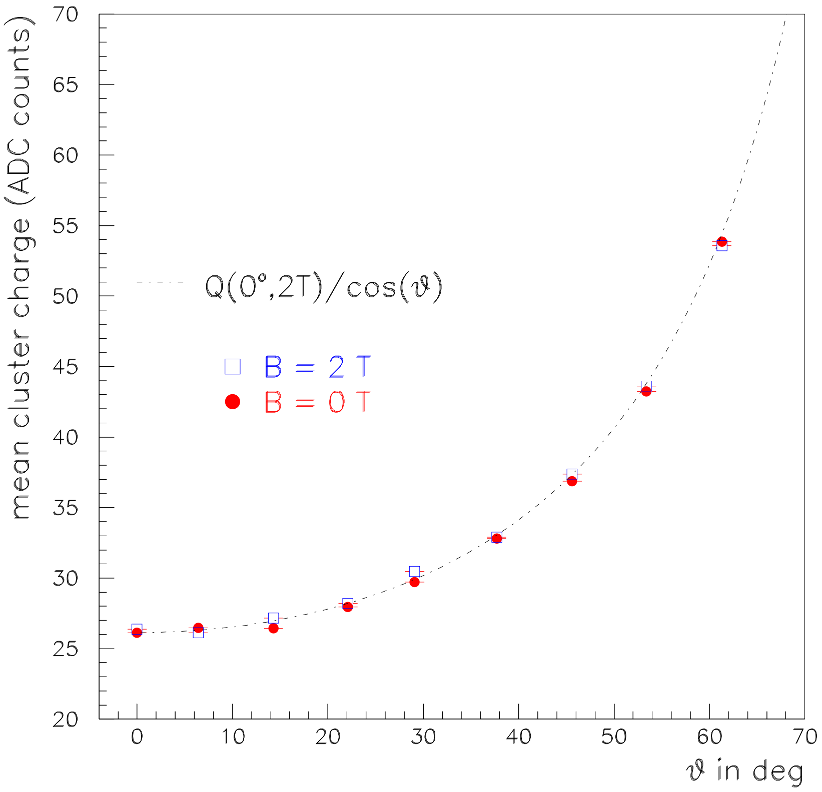

Figure 17: *The most probable value of the cluster charge distribution as a function of the incidence angle θ shown for $B = 0T$ (filled circles) and $B = 2T$ (open squares). The data show good agreement with the expected geometric scaling of the charge with $1/\cos\theta$ shown as the dashed curve.*

detector, 300 μm. The cluster size, defined as the number of strips associated to the cluster that are above the 2 σ_N threshold, is plotted in Fig. 18 for different values of the incidence ϕ angle. At $\phi = 30^o$ the number of strips in the cluster agrees with the estimate of 3.5 strips. A slight increase in the cluster size at $B = 2$T compared to $B = 0$T is observed.

The cluster charge distributions are shown in Fig. 19 for various phi angles of incidence ($B = 0$T and $\theta = 0$). The data show a slight increase but are below the expected geometric scaling of the charge by about 2 ADC counts ($\sim 7\%$) at 30^o. This is also true for the case where $B = 2$T. An attempt to understand this effect is to lower the threshold cut from $2\sigma_N$ to $1\sigma_N$. The cluster charge increased by 1.5 ADC counts for all values of ϕ between 0 and 30^o. Thus, if the threshold is lowered to 1 σ_N, the charge loss is still between 7 to 8 % at $\phi = 30^o$. This implies that the 1.5 ADC counts gained by lowering the threshold cut is mainly due to noise from the additional outlying strips. The loss of charge for tracks inclined in ϕ is not yet presently understood.

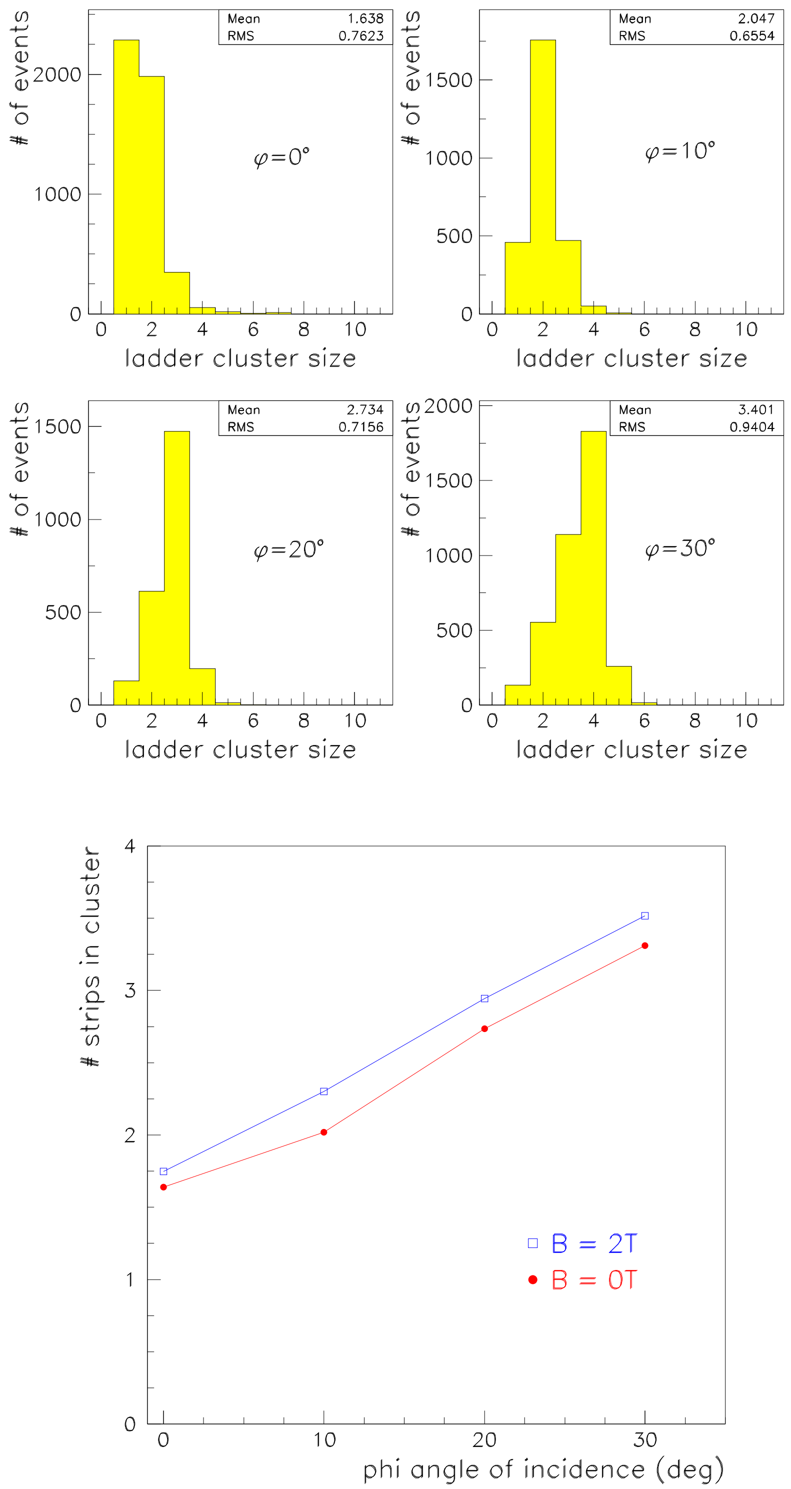

Figure 18: *(top) The number of strips in the cluster which are above the 2 σ_N threshold (B = 0T) is shown for the ladder at various values of the incidence angle ϕ. (bottom) The phi dependence of the cluster size is shown for B = 0T and B = 2T.*

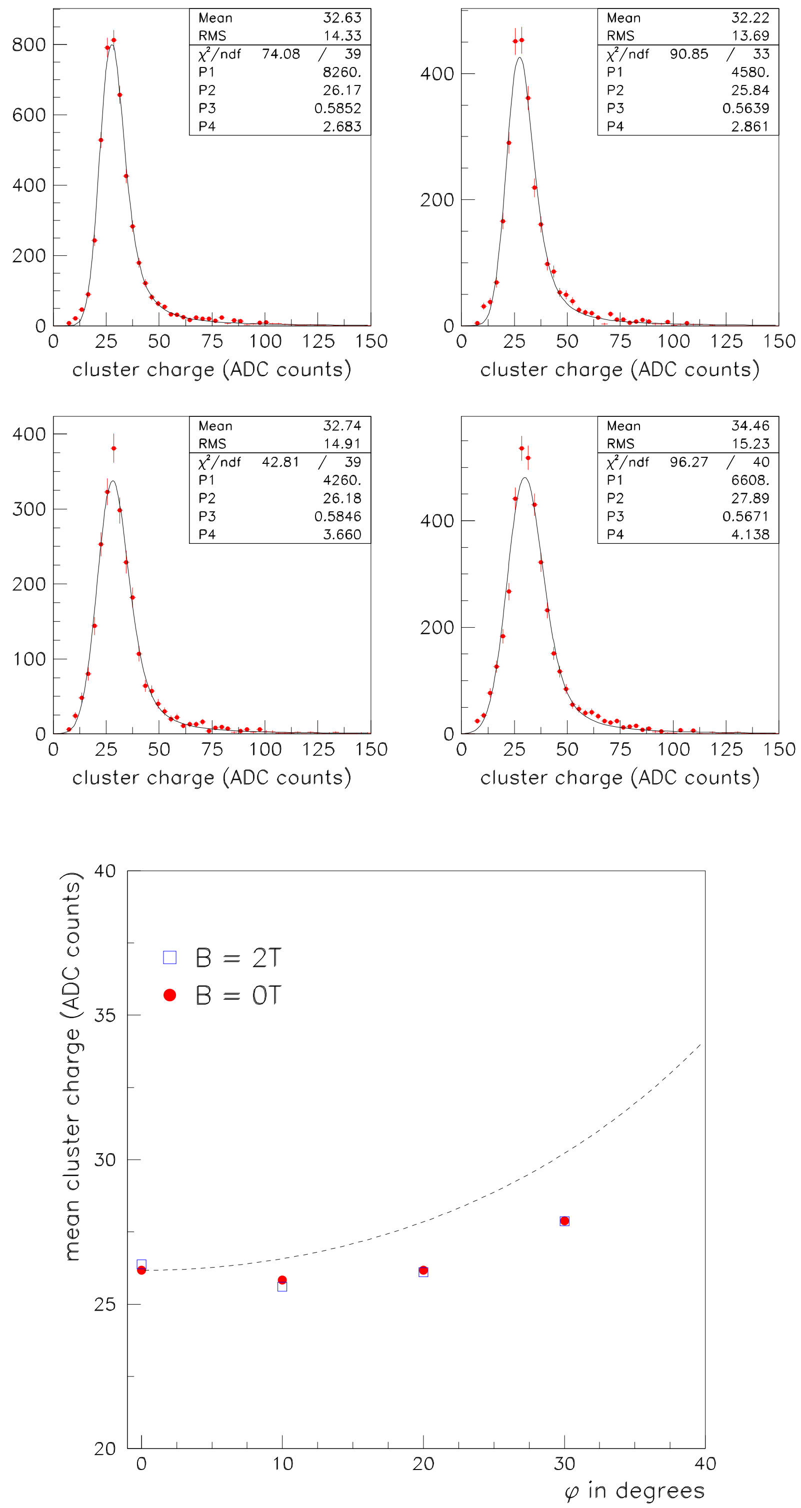

Figure 19: *(top) The cluster charge distribution for the ladder (B = 0T) is shown for various values the incidence angle (ϕ). (bottom) The phi dependence of the cluster charge ($\theta = 0$) is shown for B = 0T and B = 2T.*

7 Charge Sharing and Cluster Position

As mentioned earlier, the cluster position, y_{cog}, is calculated by summing over the strips in the cluster weighted by the strip signal with corrections for alignment and angular rotations. For non-inclined tracks, charge is divided among strips in a non-linear way[†] depending on the relative position of the impact point [3]. The parameter η for clusters with two constituent strips is defined as $\eta = (Q_R - Q_L)/(Q_R + Q_L)$, where Q_R and Q_L are the charges collected on the right hand and left hand strips, S_R and S_L, respectively. Linear charge division simply means that if the ratio of Q_L to Q_R for a two strip cluster is, for example, 0.8 to 0.2, then the impact position between the two strips using the center of gravity algorithm is given by $0.8 * S_L \; + \; 0.2 * S_{L+1}$ or $0.2 * pitch$ away from strip S_L. It can be shown, using the η parameter defined above, that there is a slight deviation from a linear charge division.

Fig. 20 shows the frequency distribution as a function of η (i.e. $dN/d\eta$ or the number of events in bins of η) for an event sample with non-inclined tracks taken with $B = 0$T. The curve shown between $\eta = \pm 0.8$ is a function proportional to $a/(1 - by^2)$. By construction

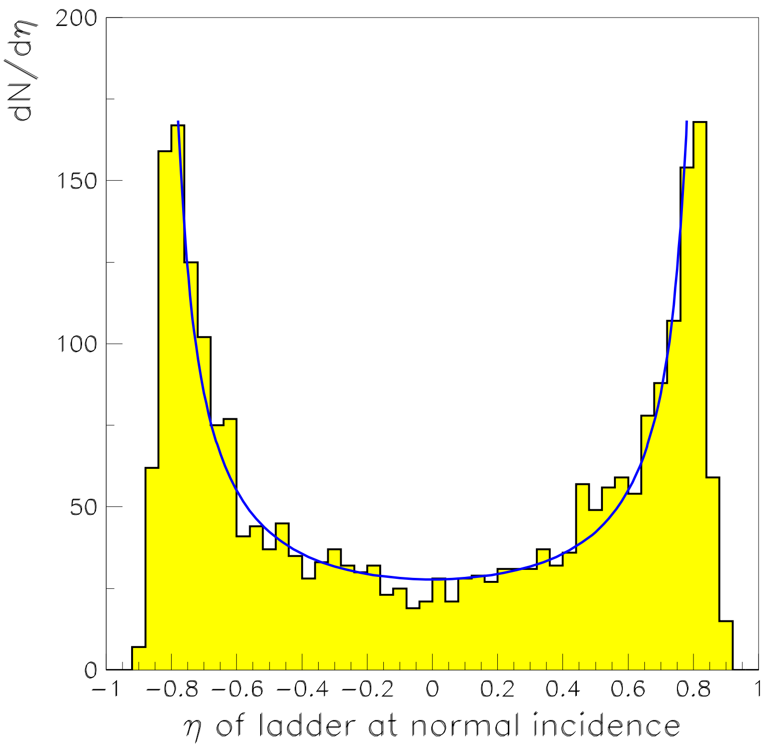

Figure 20: *Measured η distribution for the ladder for non-inclined tracks and $B =$ 0T.*

[†]A non-linear charge division may be attributed to the non-linear characteristics of the capacitive coupling between the strips.

$-1 \geq \eta \leq 1$, the values $\pm$ 1 are obtained when all the charge is deposited on either S_L or S_R. Charge diffusion and noise fill up the η region between the two peaks. A value around $\eta = 0$ indicates the the charge was equally shared between the two strips. The peaks at $\eta = \pm 0.8$ occur when charge ratio between Q_L and Q_R is 0.9 to 0.1. This is a consequence of the 2 σ_N threshold cut to separate signal from noise. A 10% charge in one of the two strips is, on average, equivalent to a charge of 2.6 ADC counts which is roughly equal to 2 σ_N.

Beam particles are triggered by a beam spot much larger than the readout pitch. One can then assume that the impact points are uniformly distributed between two neighboring strips. With the assumption that the charge sharing between two neighboring strips is independent of the total charge, the η distribution correlates the charge sharing between two strips and the impact position of the particle. The absolute y-coordinate of the particle impact position is given by $y = y_L + pitch * \int_{-1}^{\eta} \frac{dN}{d\eta}(\eta')d\eta'$, where y_L is the coordinate of strip S_L (in cm) relative to the line of reference.[‡] In the analysis, the cumulative $dN/d\eta$ distribution shown in Fig. 20 is used to obtain y for every η value. For example, a two strip cluster in the test ladder for a given event has η = -0.7. An array, in bins of η derived from Fig. 20, contains the fraction of events $dN/d\eta$ contained in each η bin from -1 to +1. Using this array the fraction of events with η between -1 to -0.7 is 0.25 which gives the measured y position to be $y_L + pitch * 0.25\ cm$. For comparison, the center of gravity method gives $y_L + pitch * 0.15\ cm$.

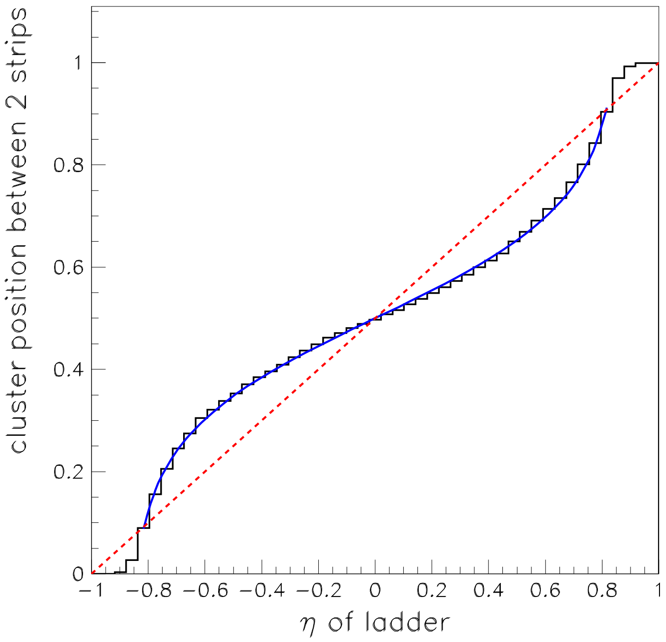

Figure 21: *Cluster position as a function of η (non-inclined tracks and $B = 0T$).*

[‡]After alignment corrections, the line of reference is defined as a line parallel to the beam axis, which goes through the exact centers of the telescope elements. Alignment and track finding will be discussed in the next section.

Fig. 21 shows the relation between the parameter η and the particle impact position y. The histogram is obtained by doing a straightforward integration of Fig. 20. The dashed line represents the impact position obtained using the center of gravity method, i.e., assuming a linear charge division. The histogram shows the deviation (up to a 10% non-linear correction) of charge sharing from a linear behavior. The curve shown is a parameterization of the cluster position as a function of η. It is derived from the the integral of $a/(1 - by^2)$ and has the functional form $y = const + c_1 \tanh^{-1}(c_2\, \eta)$.

7.1 Shape of the Charge Distribution

From the $dN/d\eta$ distribution, the shape of the charge distribution can also be derived using the method described in [3]. The corresponding charge distribution $f(-y)$ can be obtained from $dN/d\eta = (dN/dy)\,(dy/d\eta) = 1/f(-y)$, where dN/dy, as mentioned earlier, has been assumed constant between any two strips with uniform beam illumination. Using the information from Fig. 20 the shape of the charge distribution for non-inclined tracks and $B = 0$T is shown in Fig. 22. In this plot the range between ± 0.5 as shown corresponds to $\pm 25\ \mu m$ around the particle impact position, $y = 0$. The function overlaid is derived from $d\eta/dy$ where $y = const + c_1 \tanh^{-1}(c_2\, \eta)$ as obtained earlier, or $\eta \sim \tanh(y - const)$. The charge distribution shown is symmetric around the impact position with a full width at half maximum (FWHM) of 20 μm.

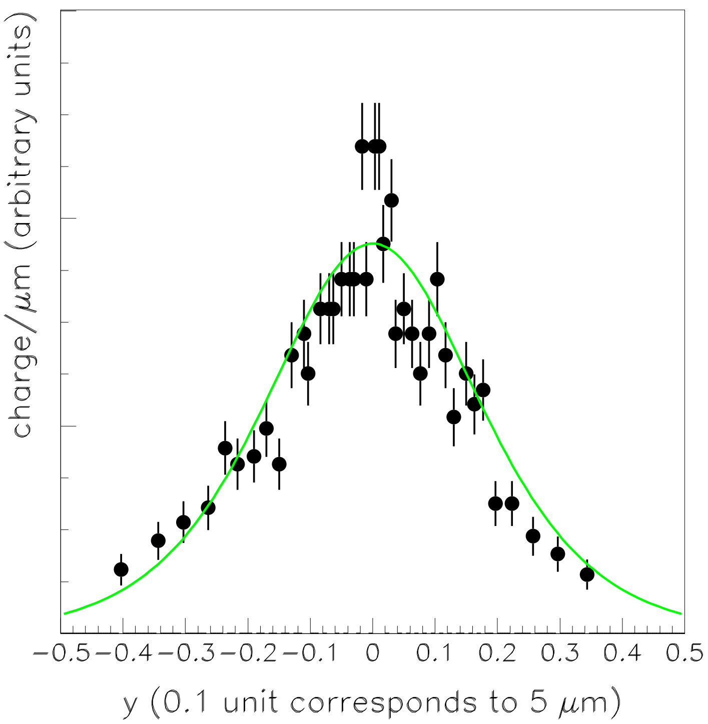

Figure 22: *Shape of the charge distribution $f(-y)$ (non-inclined tracks and $B =$ 0T).*

The method to obtain the charge distribution as described above is limited by statistics and cannot be used to obtain information on the charge diffusion beyond 0.5$*pitch$. It uses the cluster pulse height information to determine the charge distribution making this method sensitive to the S/N threshold cuts used in the analysis. In the next section, the shape of the charge distribution will be discussed again in the context of beam paritlce tracks.

We can compare the results shown above for B = 0T to the data with B = 2T. In this scenario, the charge "cloud" now drifts to the readout strips under the influence of both an electric field and a magnetic field. Similar plots are shown in Fig. 23 for data taken with the magnetic field B = 2T parallel to the direction of the strips. The left plot shows an asymmetric η distribution. The right plot shows a systematic shift of up to 15 % in the measured particle impact position. A magnetic field of 2T introduces a 12.5 μm shift in the measured coordinate of the particle impact position and a widening of the charge distribution, clearly seen in Fig. 24.

It should be noted that the B = 2T results presented here represent only a small chunk of the data. The test beam data taken with the magnetic field should be studied in more detail. The analysis of the B field data will be covered more extensively in a later report.

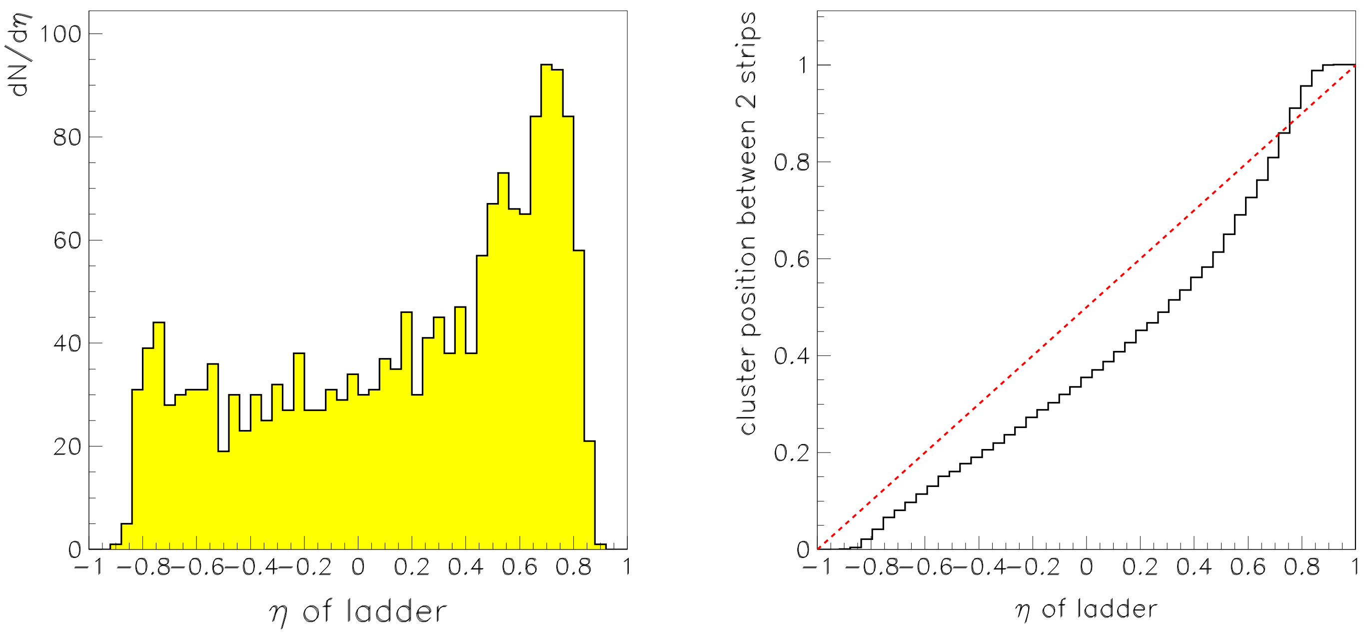

Figure 23: *For the ladder (non-inclined tracks and B = 2T): (left) The η distribution, and (right) cluster position vs η.*

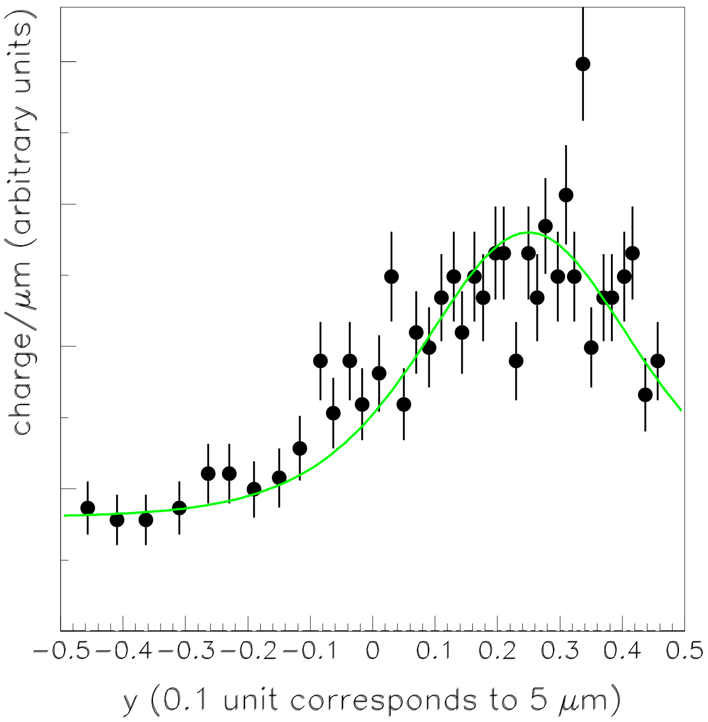

Figure 24: *Shape of the charge distribution (non-inclined tracks and B = 2T).*

8 Tracking

The silicon planes have z positions labeled z_i in Fig. 25, with i = 1,4 for the telescope elements used as anchor planes and i = 0 for the detector under study. Given a list of candidate clusters in each of the telescope element, track finding proceeds as follows. First, the offsets in y relative to the center of the first telescope element (taken as strip 192) are determined by looking at the hit correlations.

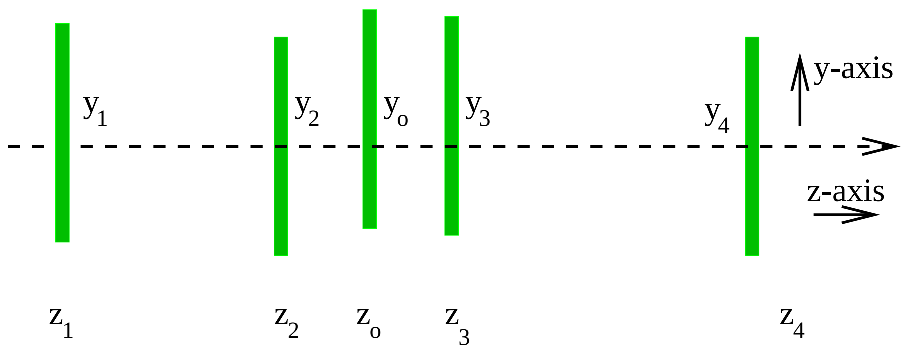

Figure 25: *The telescope elements (strips are perpendicular to the plane of the paper) used in track finding. The hit positions y_i (i=1,4) are used to determine the track parameters.*

These correlations are shown in Fig. 26 for run 3012, a sample of events where the magnet was physically moved out of the beam line and the test ladder installed in the same position z_o between TBT2 at z_2 and TBT3 at z_3. Note that the TBT2, TBT3 and the ladder were oriented in reverse relative to TBT1 and TBT4. The grid patterns are due to noisy channels and are quite significant in TBT2. By plotting the difference in hit strip numbers between these sets of detectors, we can determine the alignment offsets. These are shown in Fig. 27. The width of these distributions are proportional to the amount of multiple scattering between the two respective planes. These widths are used as constraints in the track finding. They define the size of the "road" in looking for the cluster candidates consistent with the beam particle track.

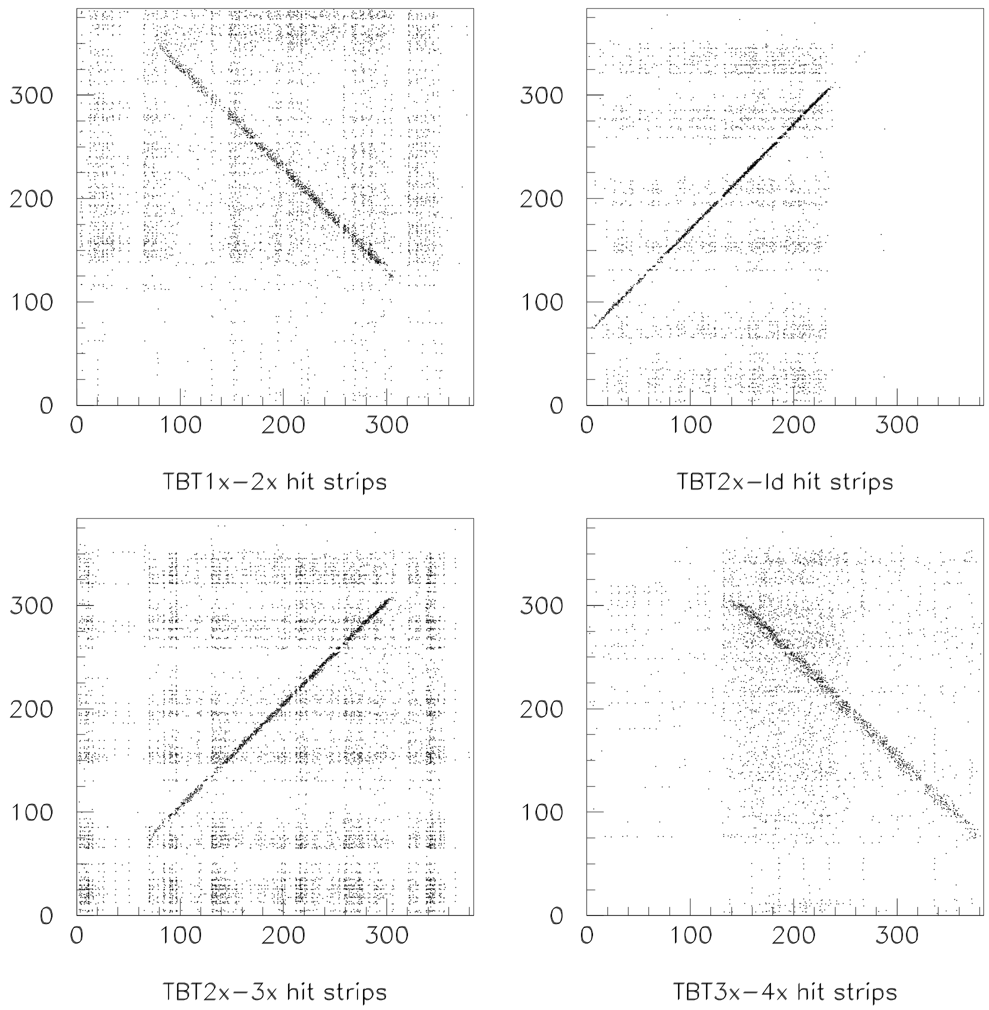

Figure 26: *Shown are the strips hit in the telescope elements and the ladder (TBT2, TBT3 and the ladder were oriented in reverse relative to TBT1 and TBT4). The x and y axis are in units of strip number going from 1 to 384.*

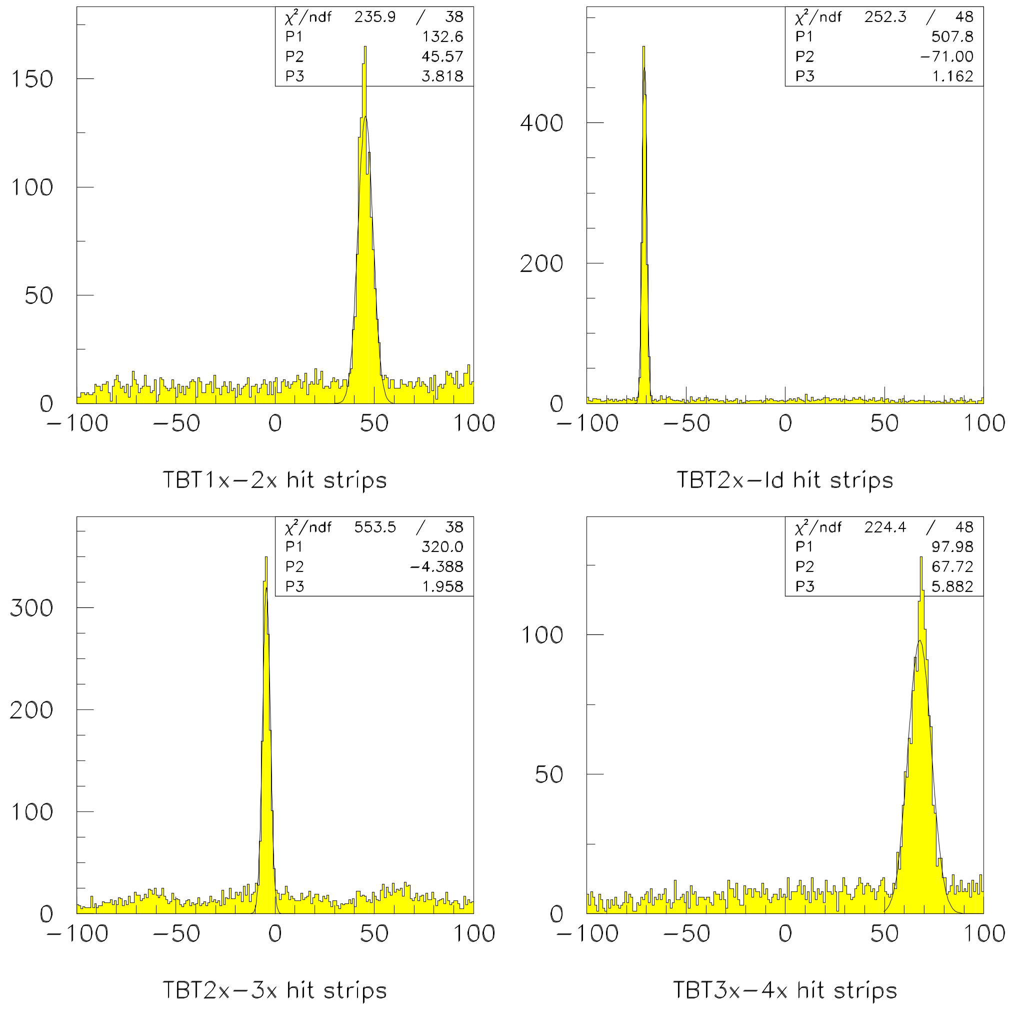

Figure 27: *The difference in hit strip numbers for the sets of planes indicated. These plots determine the alignment offsets used as constraints in the track finding. The widths of the distributions are proportional to the amount of multiple scattering between the planes.*

8.1 Hit Efficiency

Using a data sample with normally incident beam particles and $B = 0$T, events are selected by requiring a hit, consistent with a beam particle track, in each of the four v telescope elements shown in Fig. 1 (i.e. with strips oriented parallel to the x-axis). A prediction of the hit position on the test ladder is made. If a cluster is found within $\pm$ 4 strips of the predicted track position in the test ladder, this is considered a hit. The hit efficiency, defined as the ratio of the number of events with a hit in the ladder to the total number of events in the selected sample (i.e., with a track going through each of the four v telescope elements) is greater than 99.5%.

8.2 Skews and Tilts

The effect of a "skew" or a small rotation around the axis parallel to the beam is that the alignment offset varies as a function of the position along the strip length. The amount of skew can be determined by looking at the profile plot of the residual versus the orthogonal coordinates measured by the h telescopes in TBT2 and TBT3 (see Fig. 1). A tilt, on the other hand, is a small rotation around a horizontal axis perpendicular to the beam. Such a rotation will reduce the effective pitch of the detector as seen by an incoming beam particle. The amount of tilt can be determined by looking at the profile plot of the residual versus the measured y coordinate. Fig. 28 shows the variation of the residual in the test ladder as a function of the hit strip # in the h telescope of TBT2, and as a function of the hit strip # in the test ladder. The amount of skew is roughly 10 μm across 140 strips, while the amount of tilt is about 5 μm across 240 strips. These angular rotations are corrected for in the data analysis.

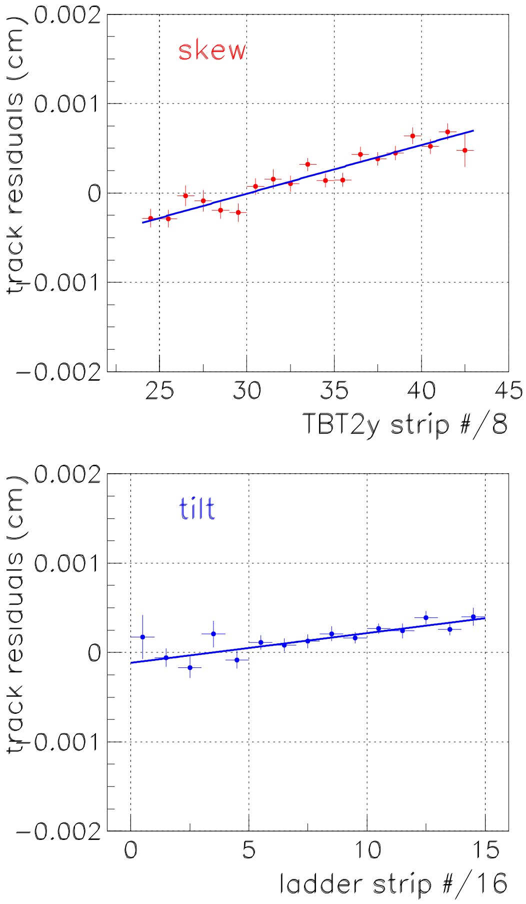

Figure 28: *(top) Track residual in the ladder versus the hit strip # in the orthogonal h detector TBT2. (bottom) Track residual versus the hit strip # in the ladder.*

8.3 Charge Distribution using Tracks

The method described in [3] has been used to obtain the shape of the charge distribution for the test ladder as shown in Fig. 22. However, this method, as mentioned earlier, is statistically limited and cannot be used to obtain information on the charge diffusion beyond 0.5$*pitch$. It is also sensitive to the S/N threshold cuts used to separate signal from noise. A more reliable method to determine the charge distribution between strips uses the track fit through the telescope elements to predict the hit position on the ladder. The hit position can typically be determined to within 10% of the readout strip pitch. The charge distribution for normally incident beam and $B = 0$T shown in the top plot of Fig. 29. The vertical axis gives the average charge in ADC counts and the horizontal axis is the distance from the hit position in cm. These plots were obtained by looping over $\pm$ 3 strips around the hit position, without applying the threshold cut. Most of the charge is collected within $\pm$ 50 μm around the hit position, with a FWHM of $\sim$ 20 ADC counts. The bottom plots in Fig. 29 show the charge distributions for the test ladder when it was rotated in ϕ, at 15^o and 30^o. These distributions are wider as expected, extending up to four strips at $\phi = 30^o$.

8.4 Track Parameters

For the setup shown in Fig. 25 the measured hit positions for a given normally incident particle track on the v telescope elements are given by y_i, i = 1,4. After correcting for the alignment offsets, a hit consistent with a particle track in each of the six detector planes, i.e. including the h elements, is required. In this note, only the case where charged tracks are normally incident to the planes and there is no magnetic field B present, is considered. In general, the detector planes, in addition to measuring the crossing point of the track will change the particle direction by multiple Coulomb scattering (MCS). The track fitting performed here does not include MCS effects.

The predicted crossing point of the track and the slope of the track at the test ladder located at z_o are given by y_o and α. The predicted hit position y_i at the ith plane can be expressed in terms of these two track parameters,

$$\tilde{y}_i \; = \; y_o \; + \; \alpha(z_i - z_o) \; = \; \sum_j a_{ij} \; p_j \tag{1}$$

where $j = 1, 2$ with $p_1 = y_o$ and $p_2 = \alpha$, and the coeficients $a_{11} = 1$ and $a_{12} = (z_i - z_o)$. Minimizing χ^2, one obtains

$$\chi^2 = \sum_i \; (y_i \; - \; \sum_j a_{ij} p_j)^2 \tag{2}$$

$$\frac{\partial \chi^2}{\partial p_k} = -2 \; \sum_i \; (y_i \; - \; \sum_j a_{ij} p_j) \; a_{ik} \; = \; 0 \tag{3}$$

$$\sum_{ij} \; a_{ij} \; a_{ik} \; p_j \; = \; \sum_i \; a_{ik} \; y_i \tag{4}$$

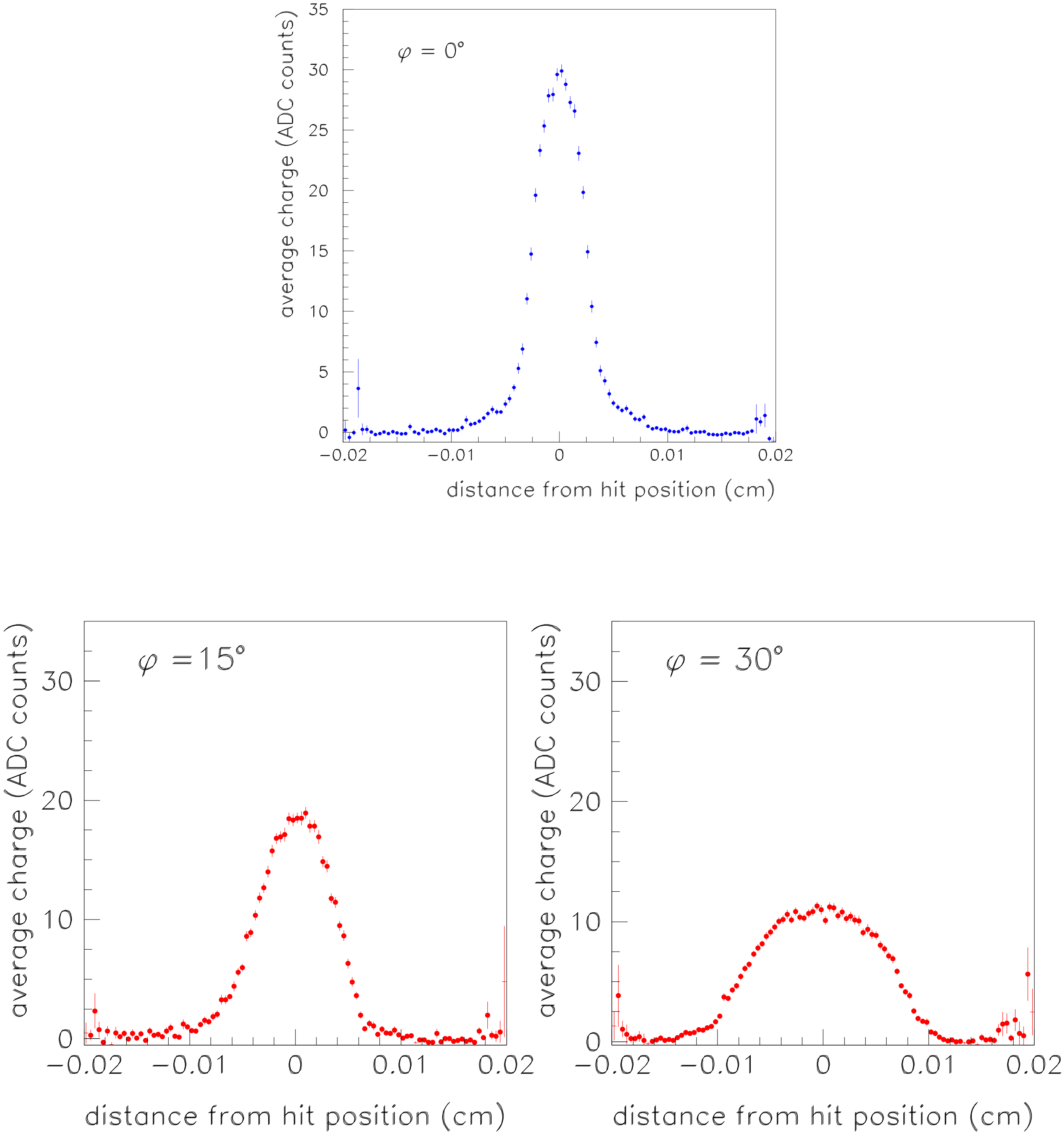

Figure 29: *Charge distribution using tracks ($\theta = 0$) for values of ϕ at 0^o, 15^o and 30^o ($B = 0T$). The plots show the average charge in ADC counts as a function of the distance from the hit position in cm.*

The left-hand side can be defined as:

$$M_{ik} = \sum_{ij} a_{ij}\ a_{ik} \tag{5}$$

$$\sum_{j} M_{ik}\ p_j = \sum_{i} a_{ik}\ y_i \tag{6}$$

$$\sum_{kj} M^{-1}_{nk}\ M_{kj}\ p_j = \sum_{ki} M^{-1}_{nk}\ a_{ik}\ y_i \tag{7}$$

Finally, we can express the track parameters p_n in terms of the measurements y_i

$$p_n = \sum_{i}(\sum_{k} M^{-1}_{nk}\ a_{ik})\ y_i = \sum_{i} c_{ni}\ y_i \tag{8}$$

8.5 Track Residuals

Using Eq. 8 the predicted crossing point of the track at the test ladder, y_o, can then be obtained from the measurements y_i as

$$y_o = c_{11}\ y_1 + c_{12}\ y_2 + c_{13}\ y_3 + c_{14}\ y_4. \tag{9}$$

The track residual, plotted in Fig. 30, is the difference between the measured hit position and the predicted crossing point at the ladder. This plot was obtained using the alignment data, taken in the latter part of the beam tests, with the magnet taken out of the beamline and the test ladder was installed in the same position z_o between TBT2 and TBT3. In order to minimize MCS effects, the track fit was performed using only the information from the silicon planes closest to the test ladder, TBT2 and TBT3. Events were selected by requiring a hit in each of the six planes consistent with a track. The track residuals shown in Fig. 30 contains the measurement errors from the intrinsic resolutions of the telescope elements and the systematic uncertainties from multiple scattering. In Fig. 31 the average track residual is plotted for various ϕ angles 0, 15 and 30^o relative to normal incidence. It should be noted that the hit position determination for clusters with greater than 2 strips has not been optimized. To improve the resolution at large incident ϕ angles, an improved cluster position reconstruction algorithm should be studied.

8.6 Unfolding the True Resolution

Using Eq. 8 the track residuals in the test ladder and in TBT2, TBT3 are given in terms of the measured (m) hit positions $y_i^{(m)}$:

$$r_o = y_o^{(m)} - 0.5027\ y_2^{(m)} - 0.4937\ y_3^{(m)}$$

$$r_2 = y_2^{(m)} - 0.1869\ y_1^{(m)} - 0.8131\ y_0^{(m)}$$

$$r_3 = y_3^{(m)} + 0.2916\ y_1^{(m)} - 0.5492\ y_2^{(m)} - 0.7425\ y_0^{(m)}$$

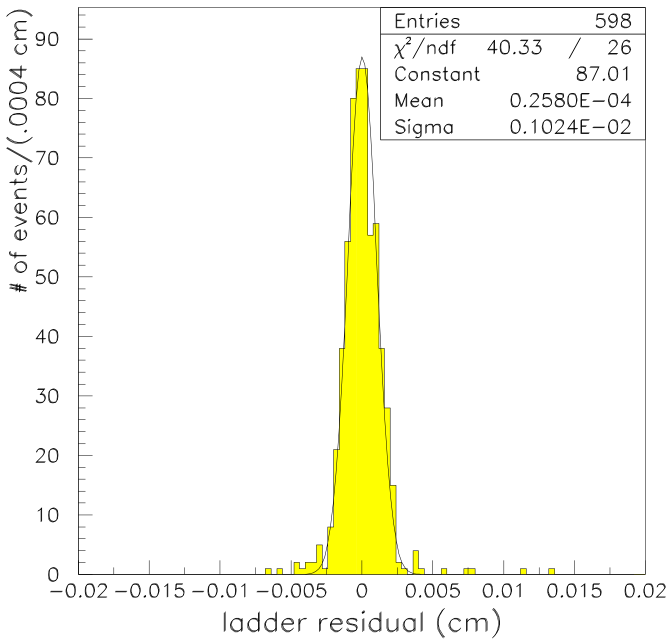

Figure 30: *Track residuals in the test ladder (using only TBT2 and TBT3) for normally incident beam particles with the magnet taken out.*

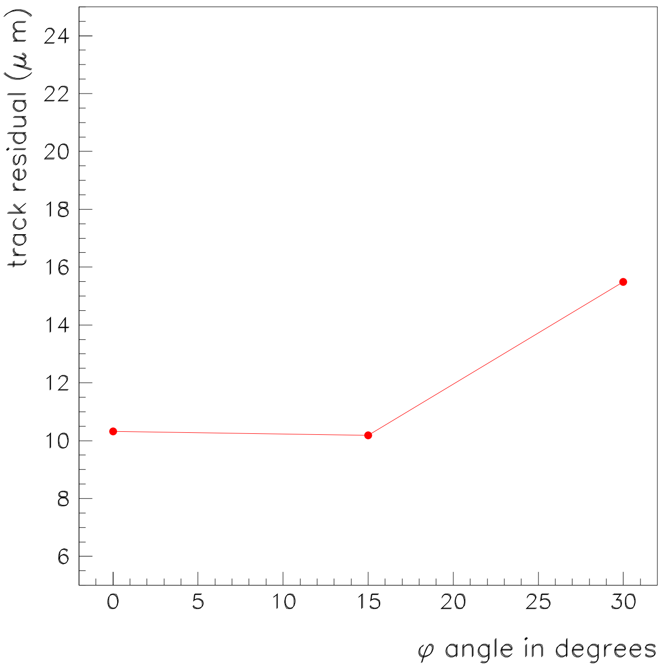

Figure 31: *Average track residual in the test ladder for various incidence angles.*

The combination of planes which gave the narrowest residual distribution for TBT2/TBT3 was chosen. TBT4 is always excluded from the track fit to minimize errors due to MCS effects. The unfolding method described in [5] has been used to determine the true position resolution. From the above equations, one obtains the width of the measured residual distribution before unfolding, δ_i^2,

$$(\delta_o)^2 \;=\; (\sigma_S)^2 \;+\; (\;0.5027^2 \;+\; 0.4937^2\;)\;(\sigma_A)^2$$

$$(\delta_2)^2 \;=\; 0.8131^2\;(\sigma_S)^2 \;+\; (\;1 \;+\; 0.1869^2\;)\;(\sigma_A)^2$$

$$(\delta_3)^2 \;=\; 0.7425^2\;(\sigma_S)^2 \;+\; (\;1 \;+\; 0.2916^2 \;+\; 0.5492^2\;)\;(\sigma_A)^2.$$

In this exercise, the reference planes are assumed to have the same intrinsic resolution $\equiv \sigma_A$. The true resolution of the studied plane is denoted by σ_S. This leaves two unknowns in the problem, σ_A and σ_S.

A χ^2 is calculated from

$$\sum_i \;(\;\delta_i^{(m)} \;-\; \delta_i^{(p)}\;)^2 \tag{10}$$

where (m) represents the measured quantity from the raw residual distribution, and (p) represents the predicted residuals resulting from the input guesses for σ_A and σ_S. The studied plane (i) resolution can be calculated from $\sigma_i^2 \;=\; \delta_i^2 - \sum_{j\neq i} c_{1j}^2\;\sigma_A^2$. Measured residuals for the detector under study contain contributions from anchor planes used in the track fit as well as from MCS effects. Contribution from multiple scattering was taken out in the χ^2 calculation by replacing $\delta_i^2 \to \delta_i^2 - (\delta_i^{MCS})^2$. The contribution δ_i^{MCS} was determined for each studied plane configuration. For the case of the test ladder, using only TBT2 and TBT3 in the track reconstruction, $\delta_i^{MCS} = 0.9\;\mu m \oplus 0.9\;\mu m$, representing the contributions due to the scattering from the silicon planes and from air.

A countour plot of the integrated χ^2, i.e., summed over all selected events, and created over a range of input values for σ_A and σ_S, is shown in the top plot of Fig. 32. A minimum is clearly seen in the highlighted region, showing the optimal range of values for σ_A and σ_S. The χ^2 distribution is shown in the bottom left corner. A cut on χ^2 below 0.05 gives the σ_A distribution on the bottom right hand side, with a peak at $\sim 8.5\;\mu m$.

The true resolution for the single-sided test ladder obtained from this exercise is shown in Fig. 33. At normal beam incidence with the magnet taken out, an unfolded resolution of 8.8 μm is obtained.

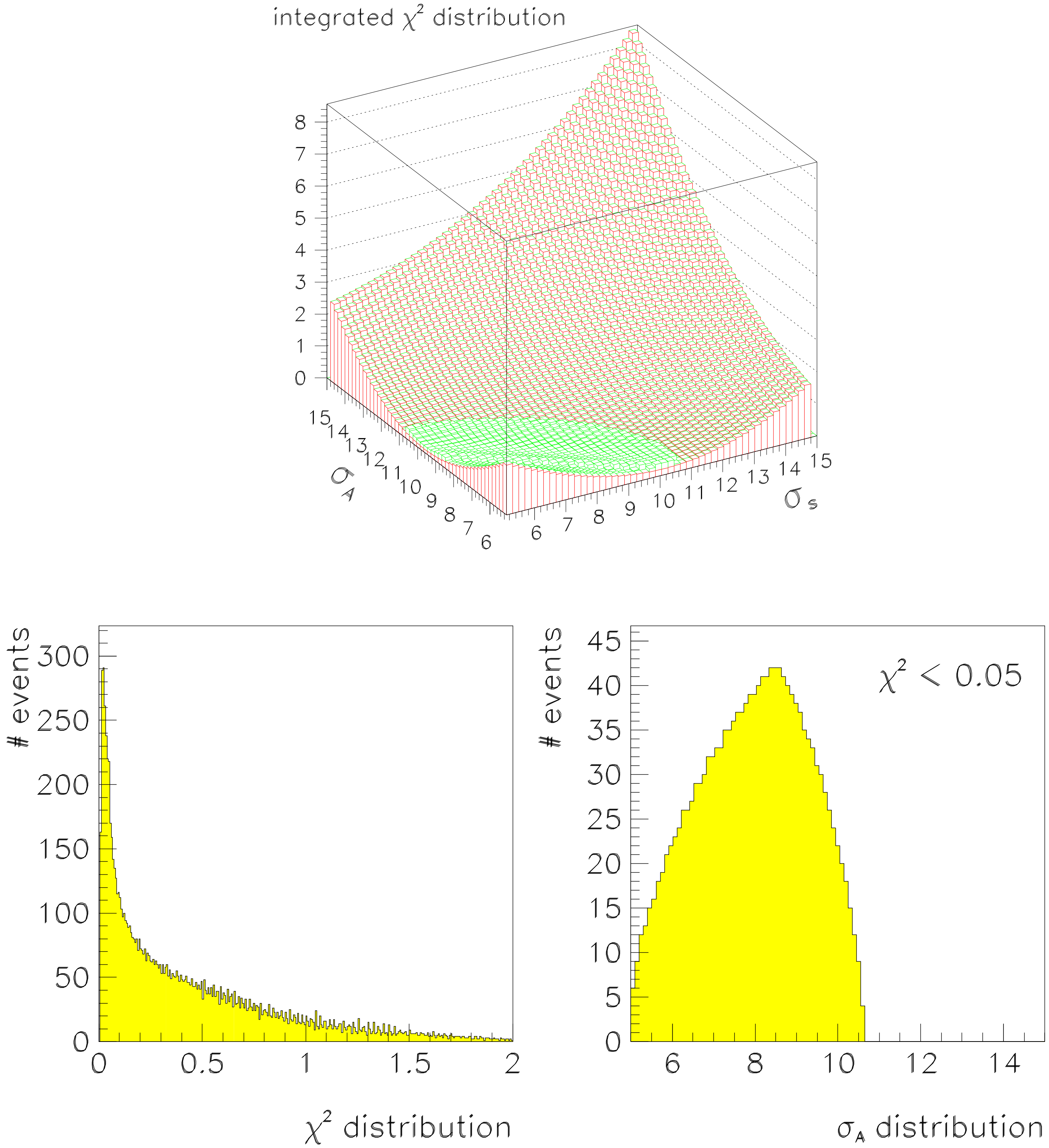

Figure 32: *(top) integrated χ^2 as a function of σ_S and σ_A. (bottom, left) χ^2 distribution and (bottom, right) the σ_A distribution is shown for events for which χ^2 is a minimum ($\chi^2 < 0.05$).*

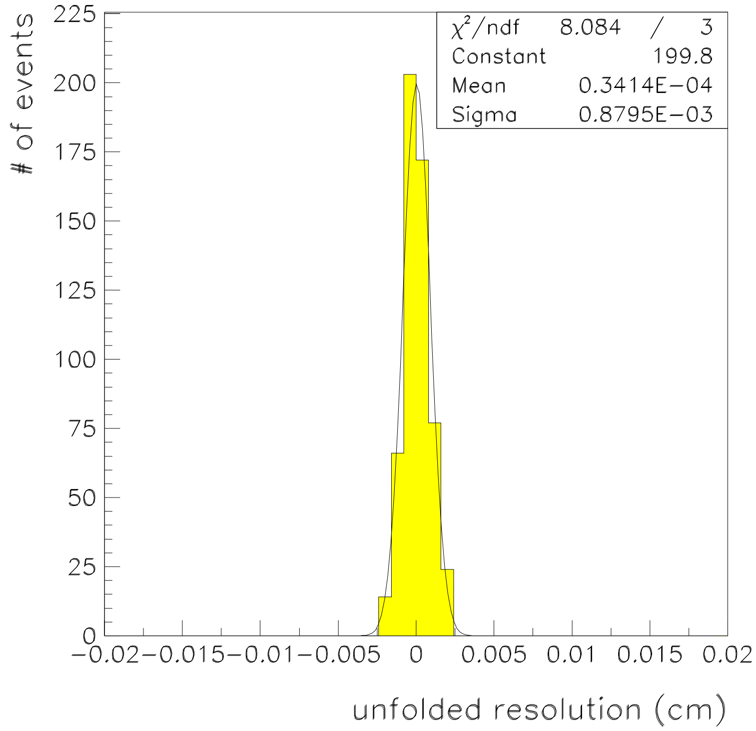

Figure 33: *Unfolded resolution of the single-sided test ladder.*

9 Irradiated Test Ladder Results

The expected radiation dose for the inner layer of the silicon tracker in Run II[§] is 0.5 MRad/fb^{-1}. In order to study the extent of radiation damage at 2 fb^{-1}, a few test detectors, some instrumented with SVX-II chips, were irradiated with 8 GeV protons at the Fermilab booster facility. The effects of the radiation damage were manifested by an increase in the detector leakage current and a change in the depletion voltage.

A single-sided ladder (see Fig. 34) which was previously irradiated up to 1 MRad ±15%, was tested. It was instrumented with SVX-II chips during irradiation. It was stored in a freezer for 4 months after irradiation. The ladder operated at a bias voltage of 120 V based on laser test stand measurements. Fig.35 shows the depletion voltage curve, where the y-axis represents the number of counts normalized to unity. The irradiated ladder shows a much slower rise compared to the non-irradiated ladder. These measurements also show that the irradiated ladder was functional at greater than 200 V bias voltage and did not show any sign of breakdown.

From the test beam data with normally incident 125 GeV charged pions, the most probable cluster charge Q_{mp} with $B = 2$T was measured to be 30 % lower compared to the

[§]During Run II the $D0$ experiment is expected to collect 2 fb^{-1} of data at 2 TeV center of mass energy.

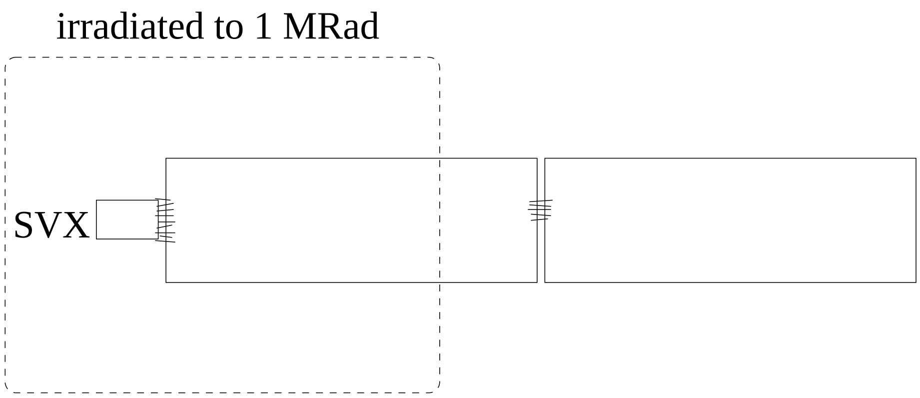

Figure 34: *A single-sided ladder previously irradiated up to 1 MRad with 8 GeV protons at the Fermilab MI-8 Booster facility. After the irradiation, the ladder was stored at room temperature for 4 months.*

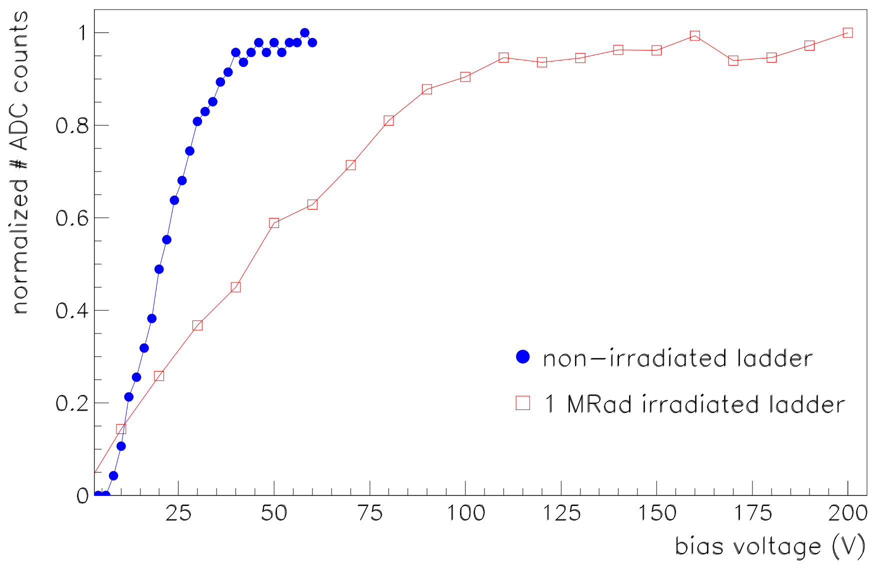

Figure 35: *Depletion voltage measurements from the laser test stand. The vertical axis is in arbitrary units normalized to one. The irradiated ladder shows a much slower rise compared to the non-irradiated ladder.*

single-sided non-irradiated ladder. It is not clear whether this deterioration is due to the irradiated ladder still operating below full depletion at 120 V or due to a degraded charge collection efficiency after irradiation [6]. The dependence of the cluster charge and noise on the chip parameter preamplifier bandwidth (PABW) was also studied. The PABW¶ is

¶For different bunch crossing or interaction times, the response or the bandwidth of the SVX-II preamplifier is adjusted by means of internal switches and capacitors to provide the optimal preamplifier output risetime and hence minimum noise.

a download parameter which allows one to set the risetime at the output of the integrator. High PABW settings correspond to longer risetimes which result in a given signal being present in the subsequent interaction interval. A lower PABW setting corresponds to a shorter risetime but the signal may be noisier than necessary. In a 132 ns interaction interval operation the proper bandwidth is chosen such that the output of the integrator reaches 99% of its final value in approximately 100 ns. The fraction of charge collected at various PABW settings, shown in the top plot of Fig. 36 for the 132 ns interaction mode, decreases with increasing risetimes. Optimum charge collection efficiency is achieved at smaller bandwidths. This is not the case for 396 ns interaction mode, where 100 % charge is collected for the full PABW range.

Radiation damage effects include an increase in the detector leakage current and a corresponding increase in noise. We observed this increase by comparing the random noise, plotted as a function of the PABW setting in Fig. 36, for both the irradiated and non-irradiated single-sided test ladders. The irradiated ladder was operated at room temperature with a leakage current of 1 μA/strip. The measured noise is consistent with being dominated by shot noise due to leakage current. At the bandwidth setting optimum for a crossing interval of 132 ns, the signal to noise ratio after about 1 MRad radiation dose is expected to degrade significantly. Assuming that after 1 $MRad$ radiation dose, 1 MIP is still 26 ADC counts at full depletion, the S/N ratio is degraded from 21 to 9 due to the increase in the random noise from 1.2 to ~ 3. It should be stated that these measurements were performed at room temperature. Detector leakage currents are quite sensitive to temperature and can be reduced significantly by operating the detectors between 0-5^oC.

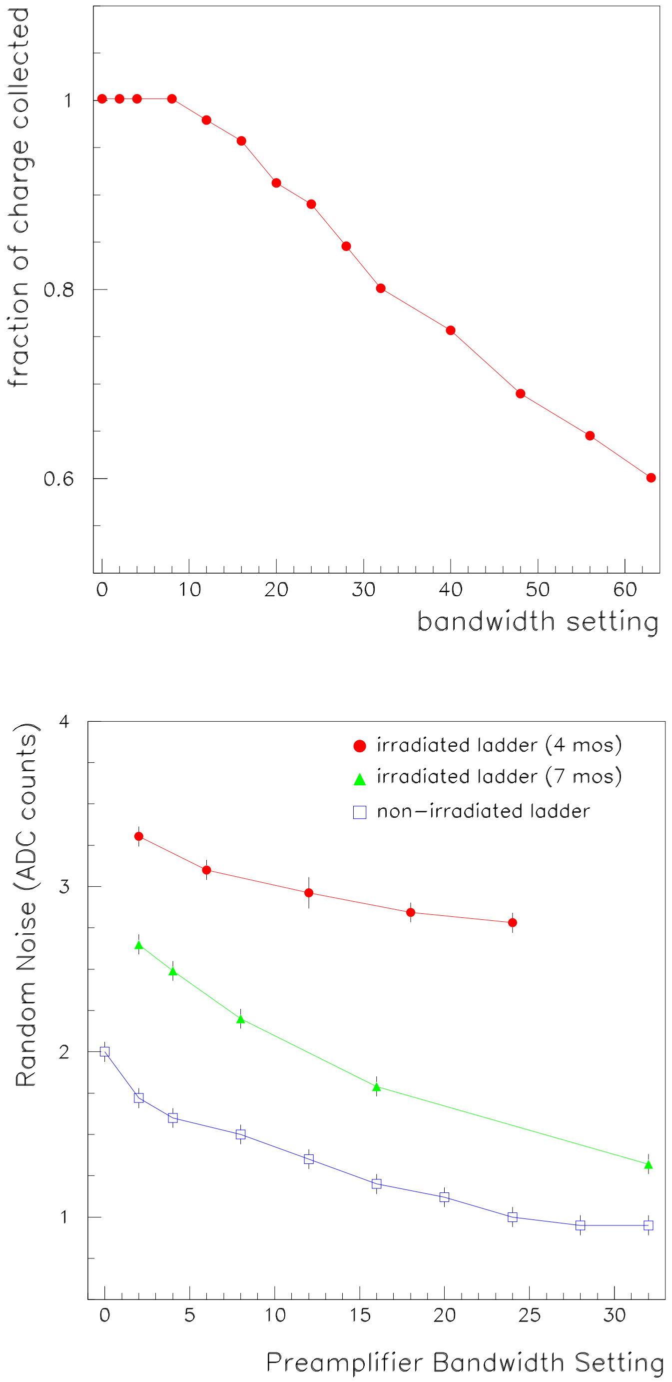

Figure 36: *(top) The fraction of charge collected decreases with higher preamplifier bandwidth (PABW, see text) settings. Optimum charge collection efficiency is achieved at smaller bandwidths. (bottom) The random noise is plotted as a function of PABW for both the irradiated and non-irradiated single-sided test ladders. Minimizing noise implies going to the largest possible bandwidth.*

10 Summary

We have performed extensive tests of the $D0$ silicon vertex system, with the final version of the SVX-II chip and the readout electronics, at a Fermilab test beam facility equipped with a 2 Tesla magnet. Under test beam conditions the system proved to work quite well. The study of the angular dependence of the cluster charge shows good agreement with the expected geometrical scaling with $1/\cos\theta$. A signal to noise ratio of 21 is obtained for the single-sided test ladders and the spatial resolution for perpendicular tracks is determined to be better than 10 μm.

Studies on radiation damage effects based on tests performed with a detector previously irradiated up to 1 MRad show a substantial increase in the depletion voltage and equivalent noise charge. Comparison with a non-irradiated ladder show that the cluster charge in the irradiated detector is degraded by as much as 30 %. From laser test stand measurements, we did not observe the breakdown of the irradiated detector for voltages up to 200 V indicating that the breakdown voltage was well above depletion voltage. The results of the beam tests give us confidence that the D-Zero silicon vertex detector will operate reliably for the duration of Run II of the Fermilab Tevatron collider.

References

[1] M. Roco, D0-Conf/97-36, Fermilab Conf/97-343-E (1997).

[2] G. Steinbrück, D0-Note 3379 (1998).

[3] E. Belau et. al., Nucl. Inst. and Meth. A 214 (1983) 253.

[4] S. Hancock et. al., Phys. Rev. A 28 (1983) 615.

[5] G. Kalbfleisch et. al., NIM A 355 (1995) 366

[6] B. Dezillie et. al., Nucl. Inst. and Meth. A 388 (1997) 314.
C. Leroy et. al., CERN-ECP/96-05 (1996).